

Spatially Aware Dictionary-Free Eigenfunction Identification for Modeling and Control of Nonlinear Dynamical Systems

David Grasev^{1,*}

¹Department of Aviation Technology, University of Defence, Kounicova 65, Brno, 100190, Czech Republic

*david.grasev@unob.cz

ABSTRACT

A new approach to data-driven discovery of Koopman eigenfunctions without a pre-defined set of basis functions is proposed. The approach is based on a reference trajectory, for which the Koopman mode amplitudes are first identified, and the Koopman mode decomposition is transformed to a new basis, which contains fundamental functions of eigenvalues and time. The initial values of the eigenfunctions are obtained by projecting trajectories onto this basis via a regularized least-squares fit. A global optimizer was employed to optimize the eigenvalues. Mapping initial-state values to eigenfunction values reveals their spatial structure, enabling the numerical computation of their gradients. Thus, deviations from the Koopman partial differential equation are penalized, leading to more robust solutions. The approach was successfully tested on several benchmark nonlinear dynamical systems, including the FitzHugh-Nagumo system with inputs, van der Pol and Duffing oscillators, and a 2-spool turbojet engine with control. The study demonstrates that incorporating principal eigenvalues and spatial structure integrity promotion significantly improves the accuracy of Koopman predictors. The approach effectively discovers Koopman spectral components even with sparse state-space sampling and reveals geometric features of the state space, such as invariant partitions. Finally, the numerical approximation of the eigenfunction gradient can be used for input dynamics modeling and control design. The results support the practicality of the approach for use with various dynamical systems.

Introduction

In recent years, the Koopman operator theory has gained popularity in the machine learning community. The theory itself was developed in the 1930s by Koopman and von Neumann^{1,2}, but it was the rapid increase of computational power that finally allowed the methods to be used for practical purposes^{3,4}. The fundamental principle is based on the transformation of the original state space of a nonlinear system to an infinite-dimensional observable space (also called lifted state space), where the evolution of the corresponding observable functions in time is described by a set of linear ordinary differential equations (ODEs)^{4,5}. For practical purposes, a finite-rank truncation (finite section) of the infinite-dimensional operator, a Koopman matrix, is sought. An alternative formulation of the goal is to find a set of nonlinear transformation observable functions, forming the basis of the lifted state space, such that the resulting linear system with prescribed dimension is sufficient for the description of the dynamics. Ideally, the original state variables should be reconstructible using a linear combination of the lifted states (observable functions). This linear system can now also facilitate the optimal control design^{3,4,6,7}.

As described in Grasev⁸, two classes of identification methods could be distinguished. The first are dynamic mode decomposition-based (DMD) methods, which utilize a predefined set of observable functions, usually polynomials and radial basis functions. The Koopman matrix is found by solving a regularized least-squares problem for the shifted time series. The basic algorithm is the extended DMD (EDMD), where the resulting Koopman matrix is an average of optimal mappings from one time step to the next, hence optimized for a one-step prediction⁹. Various alternatives and modifications exist, e.g., kernel DMD¹⁰, EDMD in reproducible kernel Hilbert spaces^{11,12}, sparse DMD aiming for the trade-off between complexity and accuracy^{13,14}, generator EDMD¹⁵, residual DMD¹⁶, symmetry-constrained EDMD for systems with multiple disjoint invariant sets¹⁷, and more. The EDMD for systems with inputs was presented in¹⁸ and further discussed in many control-oriented papers. Special category is methods based on time delay embeddings and Hankel matrices, such as in¹⁹ or²⁰, which utilize the singular value decomposition of the Hankel matrix. The prime challenge of the EDMD is the selection of observable functions for lifting. Additionally, to cope with strong nonlinearities, the libraries are often very large, scaling up to 100 functions or more. Alternatively, low-order solutions can be promoted using the above-mentioned sparsity promotion, or dictionary learning via neural networks^{21–24}. In the work of Grasev²⁵, genetic algorithms were employed to optimize the parameters of logistic functions²⁶ to find the optimal low-rank Koopman system for the gas turbine engine (GTE) dynamics. Among other disadvantages of classical EDMD are spurious eigenfunctions and ill-conditioning⁷.

The other class is spectral methods, aiming for the decomposition of the nonlinear dynamics using eigenvalues and eigenfunctions of the Koopman operator²⁷. These methods are of prime interest in this paper. The core idea is based on the proper orthogonal decomposition²⁸, where the trajectories of a system, typically evolving both in space and time, are collected and decomposed into a sum of products of three orthogonal components - spatial modes, temporal modes, and mode amplitudes. In the proper orthogonal decomposition, the modes are obtained using either the eigen-decomposition of the data correlation matrix or the singular value decomposition. In the Koopman framework, the spatial and temporal modes are given by the eigenfunctions and eigenvalues of the Koopman matrix.

The main characteristic of these approaches is that they focus on the discovery of the lifting functions, now eigenfunctions, and the Koopman matrix is given as a block-diagonal matrix of eigenvalues. Additionally, these methods sometimes also strive for a dictionary-free approach, avoiding the problems of library selection in the EDMD. Additionally, the closure problem of EDMD is overcome as eigenfunctions span an invariant subspace under the action of the Koopman operator since they are independent and can be analyzed individually (one-by-one)^{7,29}. Mezić et al. proposed a generalized Laplace analysis approach, where the eigenfunctions are generated as Laplace averages computed using nonlinear trajectories of the system's discrete-time flow map^{28,30}. The method can find exact solutions for eigenfunctions, leveraging its rigorous mathematical nature. It was shown in the latter paper that the first Laplace averages, corresponding to principal eigenvalues of the Jacobian at the fixed point, provide important information about the geometry of the dynamical system. For instance, they reveal special state-space partitions called isostables, which will also be discussed later. However, the method is suitable mostly for dissipative systems, can be ill-conditioned due to multiplication of a huge number by a very small one, and involves numerical backward integration, which can be unstable³⁰. Lusch et al. utilized a deep neural network autoencoder to find the optimal representation of eigenfunctions, applicable also to systems with continuous spectrum²². Autoencoders generally proved to be a very powerful tool when combined with the Koopman formalism. Liu et al. developed a physics-informed neural network approach, leveraging automatic differentiation for computation of the eigenfunction gradient in the eigenfunction equation cost term to enforce the solution to satisfy this equation³¹. The main downside is the limited interpretability of neural networks and potential overfitting issues. Furthermore, the training often requires a large number of samples. Kaiser et al. proposed a dictionary-based approach using the sparse identification of nonlinear dynamics (SINDy) to numerically solve the Koopman partial differential equation (KPDE) and rule out the spurious eigenfunctions often generated by the EDMD⁷. Optimal feedback control was also discussed in the paper, focusing on the utilization of the state-dependent Riccati equation. The results showed that the state-feedback control in eigenfunction space can be very effective for various nonlinear systems. The work of Grasev⁸ built on this approach, utilizing the SINDy algorithm to discover a control-affine representation of GTE dynamics. Subsequently, the autonomous dynamics were extracted and trajectories generated, and the eigenvalues were optimized by projection of the autonomous trajectories onto the span of exponential basis functions of time and eigenvalues. The spatial structure of eigenfunctions was also discovered by solving the KPDE using a dictionary of logistic functions and the adaptive momentum (ADAM) optimizer³². Finally, the optimal Koopman estimator and linear quadratic Gaussian (LQG) tracking controller were designed. Korda et al. developed a method that constructs eigenfunctions using the collected trajectories and their initial conditions, which are located on a nonrecurrent set³³. The eigenfunctions represent an optimal mapping from the space of initial conditions of the nonlinear trajectories to the space of initial conditions of observables in the lifted state space, using a set of so-called boundary functions as a basis. To supply the eigenvalues, the authors exploited the algebraic structure (lattice) of the eigenvalues of a linear DMD matrix. The paper³³ is the primary inspiration for the approach proposed in this study. However, due to its non-recurrent restriction, it is limited to dissipative systems. A new, dictionary-free method, combined with a model predictive control framework, was proposed in³⁴, which admits nonlinear input transformations while preserving the convex nature of the control optimization using Koopman predictors. The method also allows for input quantization and can exploit symmetries of the systems to speed up the optimization. The results also show a successful application to the control of systems with multiple fixed points and discontinuous eigenfunctions.

This paper proposes a new approach to the dictionary-free construction of eigenfunctions from data. The goal is to simplify the process and find samples of eigenfunctions using only the knowledge of the eigenvalues (expressing the problem only in terms of the eigenvalues). The approach can be closed in an optimization loop to find the optimal set of eigenvalues for low-rank Koopman systems. Therefore, these eigenfunctions should represent the optimal mapping, $\mathcal{F}(\mathbf{x}) : \mathbf{x}(t_0) \rightarrow \Phi_0$. The method also covers various types of dynamical systems, including systems with multiple fixed points and invariant sets, nonlinear periodic limit cycles, and input dynamics. The core idea is the utilization of a reference trajectory and corresponding Koopman modes, which will be kept constant for all trajectories. Subsequently, a change of temporal basis is performed, and the initial conditions of eigenfunctions, i.e., the values at the system's initial state, $\Phi_0 = \Phi(\mathbf{x}(t_0))$, are discovered as a regularized least-squares solution obtained by ridge regression³⁵. Additionally, the spatial structure of eigenfunctions is exploited to compute the Lie derivatives and enforce the integrity between the temporal and spatial evolution of eigenfunctions. The resulting samples can be used for interpolating or approximating eigenfunctions using suitable models. Regarding input-driven systems, the lifted input dynamics can be easily estimated using the numerically computed gradient. The approach was validated on several benchmark

nonlinear systems, including the FitzHugh-Nagumo model with inputs, the van der Pol oscillator, and the Duffing system. As an engineering case study, a two-spool turbojet engine was selected for its complex dynamics and the need to first identify a control-affine model from data before proceeding to the Koopman eigenfunction identification. Finally, an optimal tracking LQG controller was designed for the engine's spool-speed control, demonstrating the framework's applicability to control design.

Methods

Koopman operator and eigenfunctions

The Koopman operator theory provides an alternative approach to the analysis of nonlinear dynamical systems. The core principle is based on coordinate transformation of the system's state with nonlinear time evolution to a new, infinite-dimensional (functional) space of observables that are evolving linearly along the trajectories of the nonlinear system. Consider the following continuous-time autonomous system:

$$\dot{\mathbf{x}} = \mathbf{F}(\mathbf{x}), \quad (1)$$

where $\mathbf{x} \in \mathbb{R}^m$ is the state vector and $\mathbf{F} = [F_1 \ F_2 \ \dots \ F_m]^\top$ is a nonlinear drift vector field.

Further consider a generic nonlinear vector observable function, $\mathbf{g}(\mathbf{x}) \in \mathbb{C}^{n_g}$. Since states \mathbf{x} are functions of time and \mathbf{g} are functions of the states, the observable (lifted) space spanned by $\mathbf{g}(\mathbf{x})$ is infinite-dimensional. The action of Koopman operator, \mathcal{K} , on \mathbf{g} is²⁸

$$\mathcal{K}^t \mathbf{g}(\mathbf{x}) = \mathbf{g} \circ \mathbf{F} = \mathbf{g}(\mathbf{S}^t(\mathbf{x}_0)), \quad (2)$$

where $\mathbf{S}^t(\mathbf{x}_0)$ is the flow map of the system (1), giving an autonomous trajectory starting from \mathbf{x}_0 and ending at time t , and \circ denotes the composition. Thus, the nonlinear trajectory $\mathbf{S}^t(\mathbf{x}_0)$ is mapped to a new space of observables, where it exists on a hyperplane.

The family of operators, \mathcal{K}^t , parameterized by time t , is called the Koopman operator. For discrete-time systems, this time is a fixed sampling period τ (this is equivalent to discrete sampling of a continuous-time process), and the operator \mathcal{K}^τ explains the evolution from sample to sample as $\mathbf{g}(\mathbf{x}_{k+1}) = \mathcal{K}^\tau \mathbf{g}(\mathbf{x}_k)$.

The above-mentioned family of operators can be sampled from a single over-arching object associated with the continuous-time dynamics called the infinitesimal Koopman generator, \mathcal{L} . It is defined as $\mathcal{L}\mathbf{g} = \lim_{\tau \rightarrow 0} (\mathbf{g}(\mathbf{x}_{k+1}) - \mathcal{K}^\tau \mathbf{g}(\mathbf{x}_k)) / \tau$ ^{4,15}. However, for simplicity, let us stick with the notation of \mathcal{K} for continuous-time systems.

Since the operator is linear, it is reasonable to consider its spectral properties. For this, special observables, $\phi(\mathbf{x}) \in \Phi$, $\Phi : \mathbb{R}^m \rightarrow \mathbb{C}^{n_\phi}$, called eigenfunctions, are defined as

$$\mathcal{K}^t \Phi(\mathbf{x}) = \Phi(\mathbf{S}^t(\mathbf{x}_0)) = e^{\Lambda t} \Phi(\mathbf{x}_0), \quad (3)$$

where $\Lambda \in \mathbb{C}^{n_\phi \times n_\phi}$ is a block-diagonal matrix of eigenvalues of the Koopman operator, and n_ϕ denotes the dimension of the system (number of eigenfunctions).

The action of \mathcal{K} on eigenfunctions thus yields a solution to the following linear system:

$$\dot{\Phi}(t) = \Lambda \Phi(t), \quad \Phi(0) = \Phi_0. \quad (4)$$

Since the system (4) is diagonal, the space of eigenfunctions is invariant to the action of the Koopman operator represented by Λ . Finally, any observable of interest, \mathbf{g} , can be expressed in the span of eigenfunctions as

$$\mathbf{g} = \mathbf{C}_g \Phi, \quad (5)$$

where \mathbf{C}_g is the matrix of Koopman modes, where each row is a vector \mathbf{c}_j , corresponding to the j -th observable $\mathbf{g}_j = \mathbf{c}_j^\top \Phi$.

In practice, the primary demand is that the set of eigenfunctions of the finite-dimensional approximation of \mathcal{K} is a suitable basis for reconstruction of observables of interest, e.g., the nonlinear states, $\mathbf{x} \approx \mathbf{C}_x \Phi$. Fig. 1 shows the interplay between the evolution of Φ given by (4) and the original states reconstructed using the output matrix, $\mathbf{C}_{(x)}$.

The proposed approach: Spatially Aware Dictionary-Free Eigenfunction Discovery (SADFED)

Motivation

During the eigenvalue optimization that is part of Koopman model derivation in⁸, the trajectories starting from different initial conditions are projected onto the span of temporal exponential trajectories associated with a given set of eigenvalues.

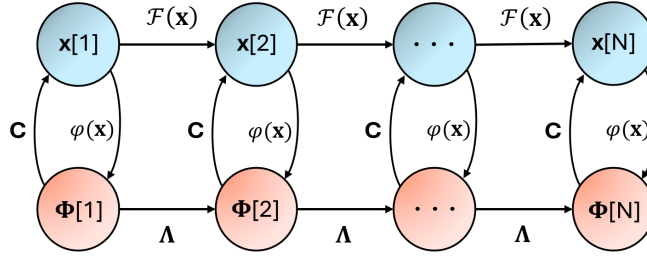


Figure 1. Schematic diagram of Koopman eigenfunction lifting and evolution.

For distinct real eigenvalues, these are purely exponential shapes. For distinct complex eigenvalues, these are multiples of exponential functions and sines and cosines, and for repeated eigenvalues, these shapes are multiplied by powers of time, forming a basis of quasi-polynomials.

In the case of 1D systems, for each initial condition, the initial conditions of eigenfunctions are assumed to be equal to 1 since the changing Koopman modes, \mathbf{C} , capture the variation of these initial conditions as a function of initial conditions of the nonlinear state, i.e., the mapping $\varphi : x_0 \rightarrow \varphi_0$ is revealed simply by plotting the exponential timeseries generated by a given eigenvalue, $e^{\lambda t}$, as a function of the timeseries of the nonlinear system's autonomous trajectories. Thus, the nonlinear autonomous dynamics of the system are explained solely using fundamental solutions of the eigenfunction system (4) with $\Phi(0) = \mathbf{I}$ and without assumptions about the spatial structure of eigenfunctions. Subsequently, the corresponding eigenfunctions can be parameterized by regressing the above-mentioned timeseries plot relation, or by numerical solution of the KPDE^{7,8}. The resulting analytical expressions for the eigenfunctions allow for analytical computation of their gradient.

However, for higher-dimensional systems, the "plotting" approach fails, and the spatial structure of eigenfunctions must be directly included in the optimization process. In other words, it is no longer possible to separate the temporal projection and eigenvalue optimization from the spatial structure discovery. Let's consider only 2D systems hereafter. For instance, consider a rectangular subdomain in the state space with the lower-left corner at the origin. Picking the upper-right corner point (maximum initial conditions) and plotting the $e^{\lambda t}$ vs $x(t)$, a curve in 3D lying on the corresponding eigenfunction manifold is obtained. However, this curve alone is indeed not sufficient for a full description of the eigenfunction's spatial structure. Therefore, a different approach is needed.

One option is to set the initial conditions as learnable parameters. However, that would increase the dimension of the parameter space. For n_t trajectories and n_φ eigenfunctions, it would yield $(n_t + 1)n_\varphi$ parameters to find. Therefore, we can instead rely on a method that leverages the linear dependence of the Koopman spectral decomposition on the initial conditions, Φ_0 , for a given set of eigenvalues and Koopman modes.

Reference trajectory and change of basis

The proposed approach is based on the selection of a reference point in the state space, \mathbf{x}_* (and the corresponding reference trajectory), setting the eigenfunctions' initial conditions to 1, and, for a single pair of complex conjugate eigenvalues, finding a reference set of Koopman modes given as

$$\mathbf{C}_{\text{ref}} = \left((\mathbf{E}\mathbf{E}^\top + \alpha\mathbf{I})^{-1} \mathbf{E}\mathbf{x}_{\text{ref}}^\top \right)^\top, \quad (6)$$

where

$$\mathbf{E} = \begin{bmatrix} e^{\alpha t} (\varphi_{R0}^{\text{ref}} \cos(\beta t) - \varphi_{I0}^{\text{ref}} \sin(\beta t)) \\ e^{\alpha t} (\varphi_{R0}^{\text{ref}} \sin(\beta t) + \varphi_{I0}^{\text{ref}} \cos(\beta t)) \end{bmatrix}, \quad (7)$$

with $\varphi_{R0}^{\text{ref}} = \varphi_{I0}^{\text{ref}} = 1$, and α is the regularization parameter. Thus, \mathbf{E} is a function of time and eigenvalues only, representing a continuous-time equivalent of the Vandermonde matrix^{28,36}.

The reference trajectory should cover a wide spectrum of dynamics of the system, ideally exploring the majority of the region of interest in the state space and/or experiencing the most prominent dynamical features of the system, e.g., both fast and slow manifolds, or invariant subsets. An unsuitable trajectory might not contain enough information to explain some parts of the state space. For some systems, the reference trajectory is the longest one.

The main idea is to fix the matrix of Koopman modes, \mathbf{C}_{ref} , obtained from the reference trajectory, and find the eigenfunctions' initial conditions for each trajectory by projecting it onto a new temporal basis given by the known exponential trajectories and modes.

Suppose the state space is $\mathbf{x} \in \mathbb{R}^m$. The decomposition of the state vector for a single complex eigenvalue, $\lambda = \alpha \pm i\beta$, is given as

$$\begin{aligned}\hat{\mathbf{x}} &= \mathbf{C}_{\text{ref}} \mathbf{E} \\ &= e^{\alpha t} (\mathbf{c}_1^{\text{ref}} \varphi_{R0} \cos(\beta t) - \mathbf{c}_1^{\text{ref}} \varphi_{I0} \sin(\beta t) + \mathbf{c}_2^{\text{ref}} \varphi_{R0} \sin(\beta t) + \mathbf{c}_2^{\text{ref}} \varphi_{I0} \cos(\beta t)),\end{aligned}\quad (8)$$

where $[\mathbf{c}_1^{\text{ref}} \ \mathbf{c}_2^{\text{ref}}] = \mathbf{C}_{\text{ref}} \in \mathbb{C}^{m \times 2}$.

Thus, for $m > 2$, the $\mathbf{c}_i^{\text{ref}}$ are column vectors of dimension $m \times 1$, and $e^{\lambda_i t}$ are row vectors of dimension $1 \times N$, where N is the number of samples. The decomposition can be vectorized, e.g., using the *reshape* function in MATLAB®, so each spectral element of the decomposition is of size either $1 \times mN$ or $mN \times 1$.

Now, it is needed to find the relation between all the remaining autonomous trajectories of the nonlinear system, starting from initial conditions different from the reference point, and the corresponding values of $\varphi_{R0}, \varphi_{I0}$. This can be derived from the expansions above by factoring out the unknown initial conditions as

$$\begin{aligned}\hat{\mathbf{x}}_{\mathbf{r}} &= [\varphi_{R0} \ \varphi_{I0}] \begin{bmatrix} \mathbf{c}_1^{\text{ref}} e^{\alpha t} \cos(\beta t) + \mathbf{c}_2^{\text{ref}} e^{\alpha t} \sin(\beta t) \\ -\mathbf{c}_1^{\text{ref}} e^{\alpha t} \sin(\beta t) + \mathbf{c}_2^{\text{ref}} e^{\alpha t} \cos(\beta t) \end{bmatrix} \\ &= \Phi_0 \mathbf{B},\end{aligned}\quad (9)$$

where $\mathbf{x}_{\mathbf{r}} \in \mathbb{R}^{1 \times mN}$ denotes the reshaped matrix of a single-trajectory data $\mathbf{x} \in \mathbb{R}^{m \times N}$.

The matrix \mathbf{B} represents a new temporal basis. It can be precomputed using the Hadamard product or a *for* loop, and the reference Koopman modes. Therefore, for each trajectory $\mathbf{x}_{\mathbf{r},i}, i = 1, 2, \dots, n_t$, the optimal eigenfunction initial values, $\Phi_0^i = \Phi(\mathbf{x}_{i,0})$, represent a projection onto the new basis \mathbf{B} (and thus coordinates of the trajectory in this transformed basis), and can be obtained via the ridge regression as

$$\begin{aligned}\Phi_0^i &= \mathbf{x}_{\mathbf{r},i} \mathbf{B}^\dagger \\ &= \left((\mathbf{B} \mathbf{B}^\top + \alpha \mathbf{I})^{-1} \mathbf{B} \mathbf{x}_{\mathbf{r},i}^\top \right)^\top.\end{aligned}\quad (10)$$

After all values of $\Phi_0 \in \mathbb{R}^{n_\varphi \times n_t}$ are obtained, the temporal projection cost function can be computed using the discovered initial conditions, Φ_0 , as

$$\mathcal{J}_{\text{temp}} = \left\| \mathbf{x}(t) - \mathbf{C}_{\text{ref}} e^{\Lambda t} \Phi_0 \right\|_F^2. \quad (11)$$

The discovered values Φ_0 are given by the projection of nonlinear trajectories onto a basis \mathbf{B} formed by functions of time and Λ . These functions are originally contained in matrix \mathbf{E} and form a fundamental solution of (4).

Spatial integrity and KPDE cost function

The eigenfunctions must also satisfy the Koopman partial differential equation given as

$$\frac{\partial \Phi}{\partial t} = \nabla \Phi(\mathbf{x}) \cdot \mathbf{F}(\mathbf{x}) = \Lambda \Phi(\mathbf{x}). \quad (12)$$

Since the mapping $\Phi : x_0 \rightarrow \Phi_0$ is an eigenfunction estimate fundamentally satisfying (4), it also reveals the spatial structure of eigenfunctions that should satisfy (12)^{7,33}. However, for complex landscapes of highly nonlinear systems, the algorithm may be prone to numerical errors, causing a local deformation of the estimated eigenfunction landscapes.

For continuous and sufficiently smooth eigenfunctions, the gradient, $\nabla \Phi_0$, can be estimated numerically using, e.g., finite differences. The drift vector field, $\mathbf{F}(\mathbf{x})$, of the original nonlinear system is either known, and thus it can be directly evaluated at each initial condition, or the derivatives $\dot{\mathbf{x}}_0$ must be computed numerically from data, which requires filtering, interpolation, and utilization of higher-order finite-difference schemes. Alternatively, the discovered eigenfunction initial conditions can be fitted by a suitable function that can be differentiated analytically to obtain the gradient.

The corresponding KPDE cost term can be computed as

$$\mathcal{J}_{\text{KPDE}} = \left\| \nabla \Phi_0(\mathbf{x}_0) \cdot \mathbf{F}(\mathbf{x}_0) - \Lambda \Phi_0(\mathbf{x}_0) \right\|_F^2, \quad (13)$$

where the gradient can be computed using, e.g., central differences as

$$\nabla \Phi_0 \approx \left[\frac{\Phi_0^+ - \Phi_0^-}{2\Delta x_1} \quad \frac{\Phi_0^+ - \Phi_0^-}{2\Delta x_2} \quad \dots \quad \frac{\Phi_0^+ - \Phi_0^-}{2\Delta x_m} \right]_{n_\varphi \times m}, \quad (14)$$

where Φ_0^+ and Φ_0^- are values of the eigenfunctions in the states being perturbed forward and backward, respectively, and

$$\Lambda = \begin{bmatrix} \alpha_1 & -\beta_1 & & & \\ \beta_1 & \alpha_1 & & & \\ & & \ddots & & \\ & & & \alpha_{n_\lambda} & -\beta_{n_\lambda} \\ & & & \beta_{n_\lambda} & \alpha_{n_\lambda} \end{bmatrix}_{n_\varphi \times n_\varphi}, \quad (15)$$

where $n_\lambda = n_\varphi/2$.

This cost function can be utilized to further promote the integrity of the solution's spatial structure by explicitly forcing the eigenfunctions $\Phi_0(\mathbf{x}_0)$ to be solutions of the KPDE. However, for less smooth or ill-conditioned eigenfunctions with complex shapes, the numerical nonlinear interpolation algorithms might fail due to rapid changes of the gradient along states, and a denser sampling of the state space might be required.

The final cost function is given by

$$\mathcal{J} = \mathcal{J}_{temp} + \gamma \mathcal{J}_{KPDE}, \quad (16)$$

where γ is a KPDE cost weighting parameter.

The optimization problem can be summarized as

$$\Lambda_{opt} = \arg \min_{\Lambda} \mathcal{J}(\Lambda), \quad (17)$$

s.t.

$$\begin{aligned} \text{Re}(\Lambda)_{\min} &\leq \text{Re}(\Lambda) \leq \text{Re}(\Lambda)_{\max}, \\ \text{Im}(\Lambda)_{\min} &\leq \text{Im}(\Lambda) \leq \text{Im}(\Lambda)_{\max}, \\ \inf \mathbf{D}(\Lambda) &\leq d_{\min}, \end{aligned} \quad (18)$$

where $\mathbf{D}(\Lambda)$ is an upper-triangular distance matrix with elements d_{ij} defined as

$$d_{ij} = \sqrt{(\Re(\lambda_i) - \Re(\lambda_j))^2 + (\Im(\lambda_i) - \Im(\lambda_j))^2}, \quad (19)$$

where $i = 1, \dots, n_\lambda - 1$, $j = i + 1, \dots, n_\lambda$, and the remaining elements are replaced by large numbers.

The last condition in (18) penalizes populations with too close eigenvalues, promoting exploration and diversity of the solution, avoiding repeated complex eigenvalues as their inclusion would require the addition of secular terms. This penalization is reasonable as it is very rare to identify repeated complex eigenvalue pairs.

The process can be divided into two parts. The first part includes the optimization of eigenvalues that minimizes the cost function in time and in KPDE by rendering good eigenfunction estimates in space. The sampling of initial conditions in the state space can initially be coarse to increase the speed of the optimization process. For more accurate gradient estimation, a nonlinear interpolation method, e.g., smoothing splines, is employed. The grid should be fine enough to allow for accurate gradient calculation using simple tools like finite differences with small perturbation methods. This process is summarized in Fig. 2.

In the second part, the original state space is sampled with high resolution, and a single computation of trajectories from the sample points is performed. These trajectories are then used to construct refined eigenfunction shapes with the already optimized set of eigenvalues. The second part is also rather computationally expensive, but it is performed only once.

Alternatively, the first part can also be performed in a two-fold manner, where the KPDE cost is initially set to zero and only the temporal optimization is performed. This leads to a faster extraction of initial eigenvalue estimates. Subsequently, the KPDE cost refinement can be performed to fine-tune the results.

This way, the eigenfunction shapes and gradients can be estimated in a dictionary-free manner using only the eigenvalues and the observed autonomous trajectories. The primary objective is to find a set of eigenvalues such that the rendered eigenfunction shapes and initial conditions minimize the joint cost function (16).

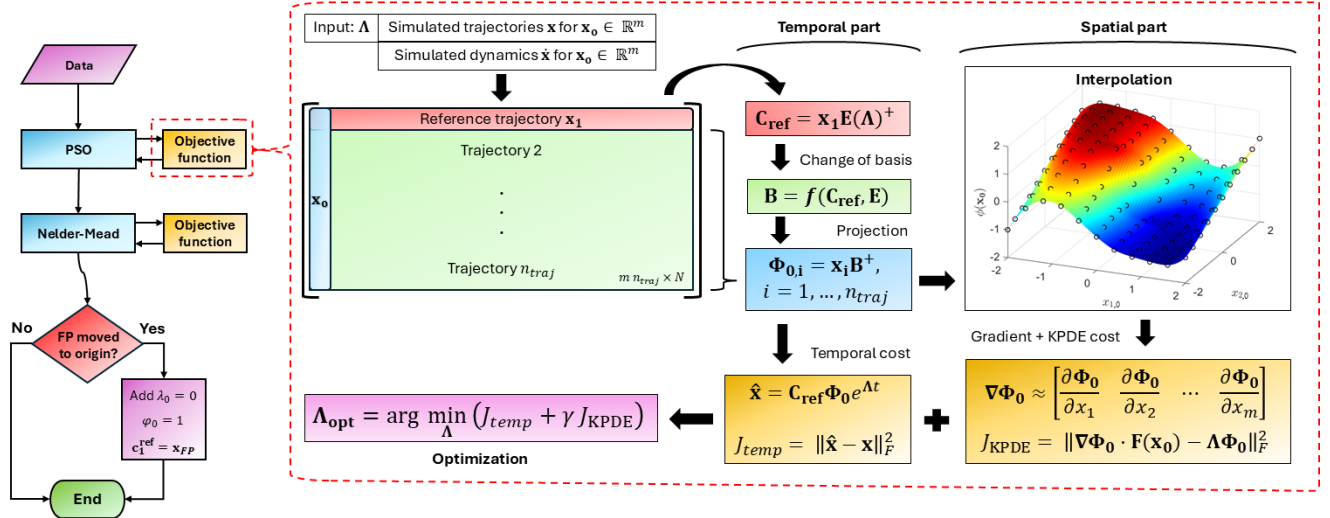


Figure 2. Flowchart of the eigenfunction identification process with the objective function.

Interpolation and input dynamics

When predicting the system's behavior using eigenfunctions, the full set of nonlinear functions must be computed only once for initialization of the eigenfunction vector. The remaining autonomous dynamics are subsequently predicted using linear operations. Thus, the eigenfunctions do not have to be represented by analytical functions, but can be represented, e.g., by a look-up table with interpolation.

Alternatively, the eigenfunction can actually be fitted by a function that minimizes not only the regression error, but also the analytically computed KPDE. For this purpose, nonlinear regression methods can be used. For instance, one can utilize a shallow neural network or extreme learning machine with a KPDE cost during learning, where the gradient can be computed using automatic differentiation. This approach is close to the physics-informed NN approach, e.g., from³¹, but now the inputs to the network training are the initial conditions in the nonlinear and eigenfunction state spaces obtained from the proposed approach. If the KPDE cost is acceptable after refinement, the numerically computed gradient can be used as training data for the fitted function's gradient, thereby minimizing $\|\Phi_0 - \hat{\Phi}(\mathbf{x}_0)\|_2^F + \|\nabla\Phi_0 - \nabla\hat{\Phi}\|_2^F$.

In the case of *controlled systems*, the gradient plays an important role as it multiplies the input dynamics in the original state space. Consider a control-affine system given as

$$\dot{\mathbf{x}} = \mathbf{F}(\mathbf{x}) + \mathbf{G}(\mathbf{x})\mathbf{u}, \quad (20)$$

where $\mathbf{F}(\mathbf{x})$ and $\mathbf{G}(\mathbf{x})$ are the drift and input vector field, respectively.

After insertion of this system into the KPDE (12), one obtains

$$\frac{\partial\Phi}{\partial t} = \nabla\Phi \cdot \dot{\mathbf{x}} = \Lambda\Phi + \nabla\Phi \cdot \mathbf{G}(\mathbf{x})\mathbf{u}. \quad (21)$$

This is a nonlinear dynamical system that can be treated as a linear parameter-varying (LPV) system. The gradient, $\nabla\Phi_0$, is already estimated over a high-resolution interpolation grid during the refinement step. If $\mathbf{G}(\mathbf{x})$ is known, it can be interpolated over the same grid. Subsequently, the entire input dynamics can be fitted by a set of suitable basis functions, replacing the expensive interpolant. For more complex gradient landscapes, one might utilize shallow neural networks or genetic programming. The input dynamics can be further fine-tuned using adjoint-based variational data assimilation and the training dataset. With the model for the input dynamics, one has the full predictor and can proceed to optimal control design.

Control design

The utilization of eigenfunction models for control was discussed in detail in the literature, e.g., in⁷, where the zero eigenfunction (conservative) was even the controlled variable as it represented the Hamiltonian. The paper mentions employing the state-dependent Riccati equation and the corresponding optimal regulators to control the eigenfunction LPV system, including an analysis of the effects of misinterpretation of eigenfunctions. Reference³³ leverages linear model predictive control (MPC) in the eigenfunction space, adding an extra term linear in the input to the autonomous predictor.

Nonlinear MPC can also be employed, specifically an adaptive or time-varying MPC, evaluating the input dynamics at each iteration of the real-time computation and fixing it for the prediction horizon, still preserving the convex nature of the MPC.

Concerning robust and adaptive control, nonlinear \mathcal{H}_∞ control approaches, e.g., based on Riccati equations as discussed in³⁷, can be adopted. Also, the Koopman model can be utilized as a nominal for the tube MPC^{38,39}. Furthermore, the dynamics can be discretized, and the adaptive LQG framework^{40,41} can be utilized in combination with a Kalman filter (KF). Since the Λ and \mathbf{C}_{ref} matrices are constant, the filter can be designed using a steady-state solution of an observer algebraic Riccati equation⁴². Details on gain-scheduled and adaptive LQG implementation can be found in the Supplementary Methods.

As mentioned above, the previous work of Grasev⁸ assessed the performance of Koopman gain-scheduled LQG for a single-spool turbojet GTE. We also discussed that targeting individual Koopman modes can help balance speed and quality of the response. Although this paper is primarily focused on identification and optimal eigenfunction discovery, the control design will be briefly discussed in the last test case - the two-spool turbojet GTE.

Summary of the framework

The summary of the entire framework is provided in Fig. 3 and the cost function computation is detailed in Algorithm 1. The process either starts with a known nonlinear dynamics, which can be utilized during the optimization, or the dynamics of the sampled system are unknown. In the first scenario, the region of interest in the state space can be sampled sparsely since the information about dynamics is accessible everywhere ($\mathbf{F}(\mathbf{x})$ is known). For the second scenario, one can take two paths. In the first one, the state space is sampled with higher resolution, the derivatives of states are computed numerically at initial conditions, and the initial values in the state space are subsequently interpolated to obtain a surrogate for the dynamics. The other path, with sparser sampling, involves data-driven identification of nonlinear dynamics using, e.g., SINDy⁴³ or variational data assimilation (adjoint gradient descent)⁴⁴. This pre-identification step significantly impacts the accuracy of the final Koopman model and also lengthens the entire process. The sampling density also depends on the smoothness of the dynamics landscapes. It is good practice to first plot the measured/computed values of time derivatives against the corresponding initial conditions of states to observe some prominent trends and shapes. This helps in deciding which of the discussed options should be utilized. For instance, smooth landscapes can be sampled sparsely, and the surrogate can be identified using regression rather than interpolation to obtain an underlying system that can be analyzed analytically. For more complex dynamics, denser sampling with interpolation might be a better choice.

Once the system dynamics are known, one can proceed to the eigenfunction identification using the proposed objective function, where the dynamics play a crucial role in the numerical gradient estimation for the KPDE cost. In this paper, particle swarm optimization (PSO)⁴⁵ and Nelder-Mead (NM)⁴⁶ algorithms were employed. PSO is a metaheuristic global optimizer that identifies promising candidates for the global minimum within the eigenvalue subspace defined by bounds of the eigenvalues' real and imaginary parts. The gradient-free NM algorithm then refines these candidates by searching locally for improved solutions.

Subsequently, for systems with a single fixed point not in the origin, the identified eigenvalues and eigenfunctions are concatenated with the zero eigenvalue and corresponding constant eigenfunction. If the fixed point is in the origin, the gradient from the refinement step can be directly utilized to construct the input dynamics in the eigenfunction space. If there are multiple fixed points, the zero eigenvalue should be included in the training population of the optimization algorithm.

The presence of invariant subsets can hamper the gradient estimation as the derivatives can explode near the separatrix, where they are, in fact, infinite. Therefore, it might be more beneficial to split the state space according to the discovered invariant subsets and fit the gradients for each subset individually. Then, after defining a margin (distance) from the separatrix, the switch can be implemented such that the dynamics in the vicinity are temporarily governed by interpolated input dynamics between the feasible regions of the gradient (at a certain distance from the separatrix, the gradients are very similar for both invariant subsets). The switch is also performed using the constant indicator eigenfunction, capturing the change of coordinates of the current attracting fixed point.

Once the input dynamics are constructed using interpolation, one might strive for a computationally less expensive approximation, e.g., an extreme learning machine or a shallow neural network, that can be trained on the interpolant knots. With the input dynamics, the Koopman eigenfunction model is complete.

The prediction is initialized using the eigenfunction interpolation once to create the vector of initial conditions of Φ . Subsequent evolution of the system is governed by linear operations for the autonomous dynamics and by the simplified approximated input dynamics, suitable for real-time evaluation and control.

This model represents an LPV model that is valid in the entire operating region of the system, not only in the vicinity of steady-state operating conditions. The model has only one parameter-dependent component - the input dynamics. Suppose the input dynamics are expressed as a linear combination of nonlinear basis functions. In that case, the model admits an affine LPV representation, which can be subsequently reformulated into a polytopic form to enable convex optimization^{47–49}. Furthermore, the optimal control design can be carried out using linear optimal control approaches such as LQG or tracking LQG. The process is as follows: Construct a grid of sample points in the state space. These sample points do not have to be

from the steady-state manifold, but can cover the entire operating region. The sampling does not have to be equidistant; it can focus on the most important parts of the state space, e.g., the admissible region bounded by safety constraints. At each grid point, evaluate the input dynamics and treat the system as locally linear time-invariant (LTI). This LTI system is inherently coherent with the underlying nonlinear dynamics, given that these are well-represented by the Koopman eigenfunctions (already validated during the identification). Find the optimal LQ controller using the corresponding algebraic Riccati equation and store the gains. Fit the gains as functions of the state variables by a suitable function, e.g., the set of input dynamics basis functions, which avoids the computation of another set of basis functions in real time. Now, the estimated nonlinear state variables are the scheduling parameters of the optimal gain-scheduled adaptive controller. Besides the input dynamics fitting, the entire process is dictionary-free.

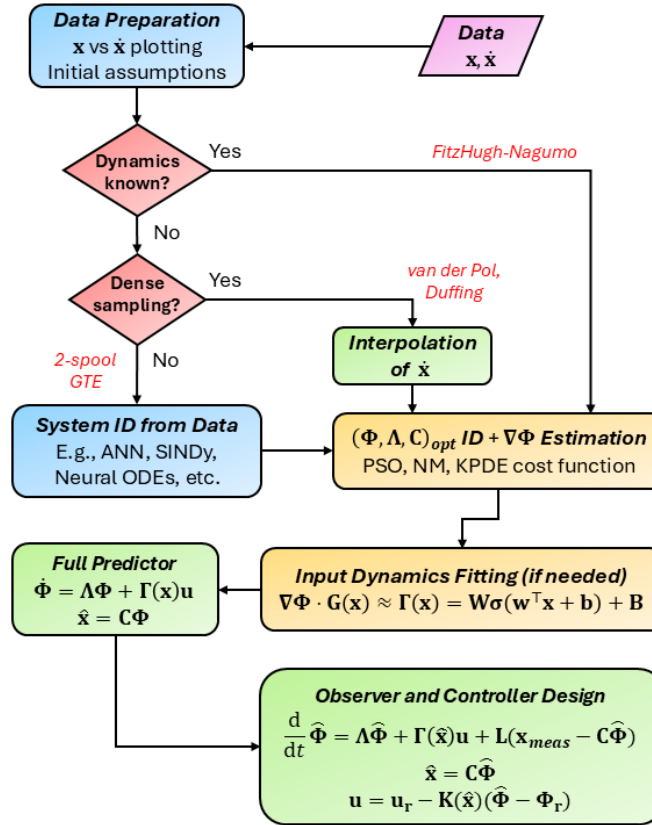


Figure 3. Flowchart of the entire framework, including the input dynamics fitting and possible control design. The example systems considered in this paper are shown as well for each case of the a priori dynamics knowledge.

Remarks

Hyperparameters The α and γ parameters might be tuned as follows: Start with small values of both parameters, perform identification, and check whether ill-conditioning or overfitting occurs (small \mathcal{J}_{temp} but large \mathcal{J}_{KPDE} , deformed eigenfunctions across initial conditions). If so, increase α until the solution is smooth/consistent. Furthermore, check the magnitude of \mathcal{J}_{KPDE} and adjust γ to approximately match the magnitude of \mathcal{J}_{temp} . Finally, tune γ according to the target error trade-off.

As the system order (i.e., number of eigenvalues) decreases, the quality of the temporal projection deteriorates, although dominant spectral components may still be identified. If the order is reduced excessively, eigenfunction solutions corresponding to the dominant eigenvalues mainly compensate for the model's limited flexibility. This is imprinted into the spatial structure of the dominant eigenfunctions, which may therefore fail to accurately capture state-space partitions such as isostables and invariant subsets, even when the principal eigenvalues are included.

With a larger number of eigenfunctions, the nonlinear trajectories can often be reconstructed accurately, mainly due to the abundance of spectral components onto whose span they are projected. However, this may come at the cost of distorting the spatial structure of the dominant eigenfunctions. In such cases, the model captures the temporal reconstruction well but fails to preserve the spatio-temporal integrity dictated by the Koopman PDE.

Algorithm 1 Eigenfunction shape and gradient estimation for optimal eigenvalues, i.e., the cost function

Input $\Lambda \in \mathbb{R}^{n_\phi}$, $\mathbf{x} \in \mathbb{R}^{n_t \times N}$

Output $J_t(\Lambda) + J_{KPDE}(\Lambda)$

$\alpha = \Re(\Lambda)$

$\beta = \Im(\Lambda)$

$\beta(\beta < 0.01) = 0$ ▷ To avoid small imaginary parts; replacing with a real eigenvalue for system order reduction

for $i = 1 : n_\lambda$ **do** ▷ Usually $n_\lambda = n_\phi/2$

$$\mathbf{E}(2i-1 : 2i, :) = \begin{bmatrix} e^{\alpha t} (\cos \beta t - \sin \beta t) \\ e^{\alpha t} (\sin \beta t + \cos \beta t) \end{bmatrix}_{2 \times N}$$

end for

$\mathbf{C}_{\text{ref}} = (\mathbf{E}\mathbf{E}^\top + \alpha \mathbf{I})^{-1} \mathbf{E}\mathbf{x}_{\text{ref}}^\top$ ▷ Computes reference projection matrix of Koopman modes

for $i = 1 : n_\lambda$ **do** ▷ Creates the new basis matrix

$$\mathbf{B}(2i-1 : 2i, :) = \begin{bmatrix} e^{\alpha_i t} (\mathbf{C}_{\text{ref}}(:, 2i-1) \cos \beta_i t + \mathbf{C}_{\text{ref}}(:, 2i) \sin \beta_i t) \\ e^{\alpha_i t} (-\mathbf{C}_{\text{ref}}(:, 2i-1) \sin \beta_i t + \mathbf{C}_{\text{ref}}(:, 2i) \cos \beta_i t) \end{bmatrix}$$

end for

for $i = 1 : n_t$ **do** ▷ Computes the initial value estimates for eigenfunctions across trajectories

$$\Phi_0(:, i) = (\mathbf{B}\mathbf{B}^\top + \alpha \mathbf{I})^{-1} \mathbf{B}\mathbf{x}(i, :)^T$$

end for

for $j = 1 : n_t$ **do**

for $i = 1 : n_\lambda$ **do** ▷ Computes the new temporal basis with the estimated initial conditions

$$\mathbf{E}_{\text{estim}}(2i-1 : 2i, :) = \begin{bmatrix} e^{\alpha t} (\Phi_0(2i-1, :) \cos \beta t - \Phi_0(2i, :) \sin \beta t) \\ e^{\alpha t} (\Phi_0(2i-1, :) \sin \beta t + \Phi_0(2i, :) \cos \beta t) \end{bmatrix}$$

end for

$\mathbf{Err}(j) = \text{mean}(\mathbf{x}(2j-1 : 2j, :) - \mathbf{C}_{\text{ref}}\mathbf{E}_{\text{estim}})$ ▷ Computes error for j-th trajectory

end for

for $i = 1 : n_{\text{traj}}$ **do** ▷ Creates the $\nabla \Phi_0 \cdot \mathbf{F}(\mathbf{x}_0)$, the LHS of KPDE

$$\mathbf{LHS}(:, i) = \begin{bmatrix} \frac{(\Phi_0^+ - \Phi_0^-)_i}{\Delta x_1} & \frac{(\Phi_0^+ - \Phi_0^-)_i}{\Delta x_2} & \dots & \frac{(\Phi_0^+ - \Phi_0^-)_i}{\Delta x_m} \end{bmatrix}_{n_\phi \times m} \cdot \begin{bmatrix} F_1(i) \\ F_2(i) \\ \vdots \\ F_m(i) \end{bmatrix}_{m \times 1}$$

end for

for $i = 1 : n_\lambda$ **do** ▷ Creates $\Lambda \Phi_0$, the RHS of KPDE

$$\mathbf{RHS}(2i-1 : 2i, :) = \begin{bmatrix} \alpha_i \Phi_0(2i-1, :) - \beta_i \Phi_0(2i, :) \\ \beta_i \Phi_0(2i-1, :) + \alpha_i \Phi_0(2i, :) \end{bmatrix}_{2 \times n_{\text{traj}}}$$

end for

$$J_{KPDE} = \text{mean}[(\mathbf{LHS} - \mathbf{RHS})^2, 'all']$$

$$J = \frac{1}{n_t} \sum_{i=1}^{n_t} \mathbf{Err} + \gamma J_{KPDE}$$

Normalization Normalization was not found to be particularly beneficial. Nevertheless, careful consideration of the \mathbf{x} range is important: the eigenfunction reference initial values, Φ_0^{ref} , should be of the same order as the grid range. Normalization to the interval $[-1, 1]$, however, remains a good practice.

Scaling In the Koopman expansion $g(\mathbf{x}) \approx \sum_j c_j \varphi_j(\mathbf{x})$ there is a reciprocal scaling invariance: for any nonzero $c_j \in \mathbb{C}$, the transformation $\varphi_j \mapsto b_j \varphi_j$ with a compensating $c_j \mapsto c_j/b_j$ leaves the representation unchanged; for complex pairs this

includes a free phase $b_j = e^{i\theta_j}$. Because the KPDE relation, $\nabla \phi_j \cdot \mathbf{F} = \lambda_j \phi_j$, is homogeneous in ϕ_j , such scaling does not alter the KPDE term. We fix $\Phi_0^{\text{ref}} = \mathbf{1}$ at the initial condition of the reference trajectory to remove the ambiguity and reduce the number of unknowns to the modes only. This also improves numerical conditioning.

Discontinuous eigenfunctions When dealing with discontinuous eigenfunctions, the gradient might explode near the separatrix. Thus, it might be important to tune the γ parameter down and let the optimization be governed primarily by the temporal projection. It also helps to clamp out large values of both terms in KPDE. Alternatively, the separatrix location can be estimated by observing trajectories in state space (e.g., via k-means clustering⁹) or by first running the optimization with $\gamma = 0$ and plotting level sets of the first eigenfunction. Subsequently, the separatrix can be parameterized, and the distance from it can be computed. Only points at a sufficient distance from the separatrix can be subsequently utilized for the calculation of the gradient and $\mathcal{J}_{\text{KPDE}}$.

Symmetry If the system of interest exhibits strong symmetry in state space, this symmetry can be exploited. The state space may be sampled only at its half- or quarter-subspaces. This subspace does not have to contain all distinct fixed points, as, due to the symmetry, the dynamics information around one fixed point gives the information around the other. This can help reduce the computational cost of the optimization step.

Zero eigenvalues for a single fixed point In case of a single fixed point that is not in the origin, it can either be shifted to the origin by subtracting its coordinates, or the conservative eigenvalue, $\lambda_0 = 0$, must be included in the population. In the former case, the set of eigenfunctions is subsequently concatenated with $\phi_0 = 1$ as $\Phi = [\mathbf{1} \ \Phi_0]$, the eigenvalues are concatenated with $\lambda_0 = 0$ as $\Lambda = \begin{bmatrix} 0 & \Lambda_{\text{opt}} \end{bmatrix}$, and the reference modes are concatenated with modes directly given by the coordinates of the fixed point as $\mathbf{C}_{\text{ref}} = [\mathbf{x}_{\text{fp}} \ \mathbf{C}_{\text{ref}}]$. This way, the first eigenfunction stays constant, and its role in the state reconstruction is to capture the offset given by the fixed-point coordinates. However, the rest of the eigenfunctions and their gradients must be subsequently interpolated/approximated on the original grid (with no fixed-point subtraction). The latter approach allows for direct identification of the constant eigenfunction together with the other ones. The eigenfunction ϕ_0 also serves as a sanity check, as it should be very close to 1 everywhere. For systems with multiple fixed points and invariant manifolds, this eigenfunction serves as an "indicator" function to tell in which invariant subset the point in the state space is located¹⁷.

Sensitivity analyses Sensitivity analyses and scaling effects of varying hyperparameters will be presented for the FitzHugh-Nagumo example in the following section.

Results

System with closure and exact eigenfunctions

The first investigated system is a well-known example of a system that satisfies finite Koopman closure - it has a closed observable subspace for a finite-dimensional Koopman operator. The system is given as

$$\begin{aligned} \dot{x}_1 &= \mu x_1 \\ \dot{x}_2 &= \nu(x_2 - x_1^2), \end{aligned} \tag{22}$$

where μ and ν are the principal eigenvalues.

The system has a single fixed point at $(0,0)$ and admits a closed Koopman observable subspace with observables constructed as $\psi_1 = x_1$, $\psi_2 = x_2$, and $\psi_3 = x_1^2$. The system is closed, since $\dot{\psi}_3 = 2x_1\dot{x}_1 = 2\mu x_1^2 = 2\mu\psi_3$. For the parameters given as $\mu = -0.1$ and $\nu = -1$, the linear Koopman system is

$$\frac{d}{dt} \begin{bmatrix} \psi_1 \\ \psi_2 \\ \psi_3 \end{bmatrix} = \begin{bmatrix} -0.1 & 0 & 0 \\ 0 & -1 & 1 \\ 0 & 0 & -0.2 \end{bmatrix} \begin{bmatrix} \psi_1 \\ \psi_2 \\ \psi_3 \end{bmatrix}, \tag{23}$$

and the exact eigenfunctions, computed using normalized right eigenvectors of the system matrix, are given as $\phi_1 = x_1$, $\phi_2 = 1.6x^2$, and $\phi_3 = x_2 - 1.25x_1^2$.

The trajectories were simulated starting from a grid of 21×21 evenly distributed initial conditions in the range of $[-1, 1] \times [-1, 1]$. The Heun numerical integration with a time step of $\Delta t = 0.2$ s was employed. The trajectories were simulated for 50 seconds, yielding 250 time samples for each. All simulations in this paper were performed in MATLAB R2022a software and on an Acer Nitro AN515-54 notebook with OS Microsoft Windows 10 Home, processor Intel(R) Core(TM) i5-9300H 2.40 GHz (8 CPUs), GPU NVIDIA GeForce GTX 1650 8GB, and 8 GB RAM.

For the temporal projection error computation, only every second odd rows and columns were used as depicted in Fig. 4. The reference trajectory started from the point $[-1, -1]$ as it is the longest trajectory, covering both the slow parabolic manifold and the fast convergence to it.

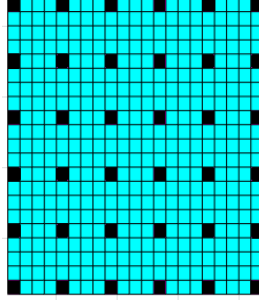


Figure 4. Sparse selection of trajectories from the full 21×21 (blue) grid to 6×6 (black) grid using every second odd rows and columns.

The principal eigenvalues, $\lambda_1 = -0.1$ and $\lambda_2 = -1$, were included in the population and fixed for all generations. Two more eigenvalues were optimized using the mixed PSO-NM algorithm with the PSO population size set to 50 and the number of generations set to 200, which was also set for the rest of the upcoming examples. The initial population was generated using the *hypercube sampling function*. The number of NM iterations was set to 1000. The regularization and KPDE cost parameters were set as $\alpha = 10^{-6}$ and $\gamma = 10^{-4}$, respectively. The upper bound for real parts was set to -0.1 . Resolution of the interpolation grid for the gradient estimation was 100×100 ($\Delta \mathbf{x} = [0.02, 0.02]$).

The resulting temporal cost was $\mathcal{J}_{temp} = 1.24 \times 10^{-9}$ and the KPDE cost was $\mathcal{J}_{KPDE} = 0.048$. The fitted trajectories are plotted in Fig. 5.

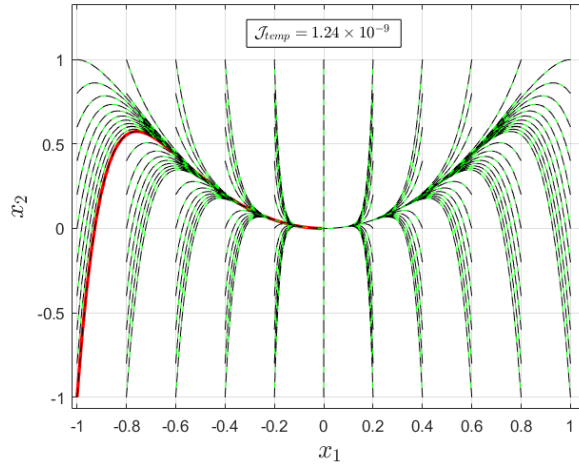


Figure 5. Fitted trajectories in the state space - ground truth (green solid) vs. fitted (black dashed). The red line highlights the reference trajectory. Only samples corresponding to odd rows and columns are plotted for clarity.

To show the effect of a different reference trajectory, when the trajectory starting from $[1, 1]$ was selected, the resulting costs were $\mathcal{J}_{temp} = 2.06 \times 10^{-5}$ and $\mathcal{J}_{KPDE} = 0.22$, yielding significantly worse performance.

The discovered optimal eigenvalues were $\lambda_1 = -0.1$, $\lambda_2 = -0.182 \pm 0.01i$, $\lambda_3 = -0.34$ and $\lambda_4 = -1$. The second eigenvalue got close to the exact eigenvalue $2\mu = -0.2$. In Fig. 6, the discovered eigenfunctions ϕ_1 , ϕ_2 , and ϕ_4 are compared to the exact ones, normalized to start from 1 at the upper-right corner as the reference eigenfunctions. The discovered eigenfunctions closely match the exact ones, with the discrepancies given by the presence of the small imaginary part in λ_2 .

Shifted fixed point: FitzHugh-Nagumo system with inputs

The control-affine FitzHugh-Nagumo model with inputs was selected to show that the numerically computed eigenfunction gradient can be directly utilized for modeling of the lifted input dynamics. The system is given as

$$\begin{aligned} \dot{x}_1 &= -x_2 - x_1(x_1 - 1)(x_1 - \alpha) + \beta + u, \\ \dot{x}_2 &= \gamma(x_1 - \delta x_2) + \cos(x_1^2)u, \end{aligned} \tag{24}$$

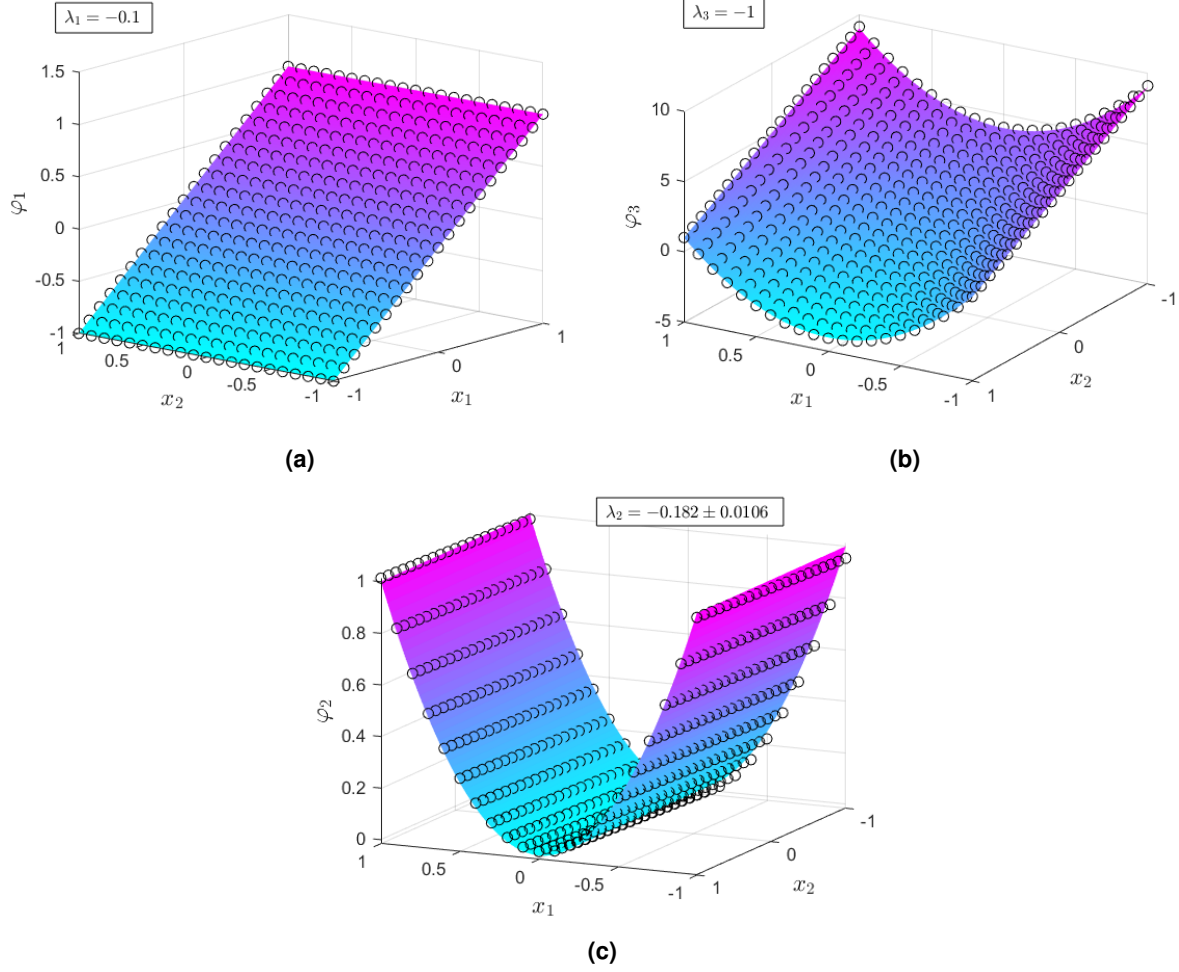


Figure 6. Exact (colored surfaces) vs. estimated (black circles) eigenfunctions - (a) ϕ_1 , (b) ϕ_2 , and (c) ϕ_3 . Eigenfunctions were normalized to start from $\phi_i(1, 1) = 1$.

where u is the input variable, and the parameters were set as $\beta = 0.05$, $\gamma = 0.2$, $\delta = 1$ and $\alpha = 0.5$.

The system was first simulated using the autonomous part ($u = 0$). The Heun numerical integration was utilized with a time step of $\Delta t = 0.1$ s. The grid of 21×21 initial conditions was constructed in the range of $[-1, 1.5] \times [-1, 1.5]$. Each trajectory was 20 seconds long (i.e., 200 time samples), ensuring that the fixed point was reached after entering the slow manifold. The total size of the dataset was $(2 \times 21^2) \times 200 = 88200$. The reference trajectory started from the point $[-1, -1]$ as it covers a fair portion of the state space as well as both the slow manifold and the fast oscillatory convergence phase (see Fig. 7). The fixed point is $\mathbf{x}_{FP} = (0.0345, 0.0345)$, and, for the given parameters, the Jacobian matrix is

$$\mathbf{J} = \begin{bmatrix} -0.4 & -1 \\ 0.2 & -0.2 \end{bmatrix}, \quad (25)$$

and the corresponding principal eigenvalues are $\lambda_{12} = -0.3 \pm 0.436i$.

Since the fixed point is not in the origin, its coordinates were subtracted from the trajectories for the temporal part and added back for the interpolation in the KPDE part. The reason is that the nonlinear input dynamics, $\mathbf{G}(\mathbf{x})$, must be evaluated on the original unshifted grid. Seven additional eigenvalues were optimized by the algorithm and concatenated with the principal eigenvalues. After the optimization, the constant eigenfunction, the zero eigenvalue, and the corresponding mode amplitudes were included in Λ , Φ_0 and \mathbf{C}_{ref} , respectively.

The parameters were set as $\alpha = 10^{-6}$ and $\gamma = 10^{-4}$. The PSO population size was set to 100, and the NM was performed for 1000 iterations. The interpolation grid size for identification was 100×100 ($\Delta \mathbf{x} = [0.025, 0.025]$). The algorithm converged to an optimal solution with the total cost of $\mathcal{J} = 1.813 \times 10^{-6}$. The temporal cost was $\mathcal{J}_{temp} = 7.67 \times 10^{-7}$. Once the optimal

(Λ, Φ_0) set was found, the refinement was performed using 125×125 trajectories in the range $[-1, 1.5] \times [-1, 1.5]$ and an interpolation grid of 500×500 points ($\Delta \mathbf{x} = 0.005$). The autonomous trajectories are depicted in Fig. 7.

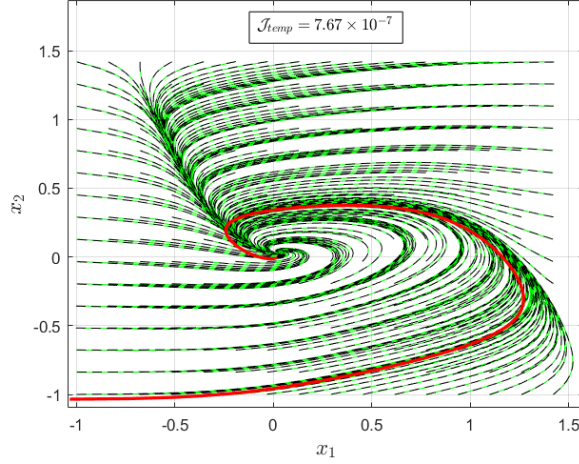


Figure 7. Fitted autonomous trajectories of the FitzHugh-Nagumo system - ground truth (green solid), fit (black dashed), reference trajectory (red solid).

The prediction with the input dynamics was first evaluated using linear interpolation of the gradient data computed during the post-identification refinement step. The nonlinear input dynamics are $\mathbf{G}(\mathbf{x}) = [1 \quad \cos(x_1^2)]^T$. The results showed that the prediction was very accurate, with the sum of mean absolute errors (MAE) in both states being $\sum \text{MAE} = 0.0128$, where $\text{MAE} = |\mathbf{x} - \hat{\mathbf{x}}|$, proving the sufficiency of the numerically computed gradient.

However, even the linear interpolation is too computationally intensive for practical purposes. Thus, the eigenfunction input dynamics, $\nabla \Phi \cdot \mathbf{G}(\mathbf{x})$, were approximated as a whole by a linear combination of selected basis functions, resulting in a much more compact model. The basis functions were sigmoid functions given as

$$\sigma(\mathbf{x}, \mathbf{w}, \mathbf{b}) = \frac{1}{1 + e^{-\mathbf{w}\mathbf{x} - \mathbf{b}}}, \quad (26)$$

where \mathbf{w} and \mathbf{b} are the weights and biases, respectively.

The optimization was carried out using the MATLAB Deep Learning Toolbox, enabling quick design of the model in the form of an extreme learning machine with a linear output layer and training on the GPU. The ADAM optimizer was utilized for the optimization. Fig. 8 depicts the results of prediction using the approximated gradient. The accuracy got worse by 170 %, but was still deemed acceptable with $\sum \text{MAE} = 0.0347$.

Example sensitivity analyses

Sensitivity analysis was carried out for the FitzHugh-Nagumo example. Effects of hyperparameters and grid dimensions on the accuracy and computational time are briefly discussed.

- Effect of wrong choice of reference trajectory.** As for the previous system, the identification was also carried out using a different reference trajectory starting from the $[1.5, 1.5]$ point. All the identification settings were kept the same. Despite the trajectory being a tempting choice as it starts from the furthest corner of the grid, the resulting errors were $J_{temp} = 1.2 \times 10^{-6}$ and $J_{KPDE} = 0.1191$, so an order of magnitude worse than for the $[-1, -1]$ trajectory.
- Scaling with varying grid dimensions.** The effects of (i) the number of eigenvalues, (ii) the subgrid utilized for computation of the temporal cost, (iii) the size of the full grid of initial conditions, and (iv) the interpolation grid used in the identification, on the computational time, J_{temp} , and J_{KPDE} were analyzed.

The effects of α and γ are shown in Fig. 9. With increasing γ , the algorithm puts more emphasis on minimizing the KPDE cost, leading to an increase in the temporal cost. Thus, an optimal trade-off is of interest. With increasing α , the numerical stability increases (avoiding ill-conditioning and overfitting), and both error terms grow.

The effect of grid sizes and the number of eigenvalues is depicted in Fig. 10. Grid sizes have the most influence on the computational time. With the increasing number of subgrid points, the algorithm puts more weight on the overall

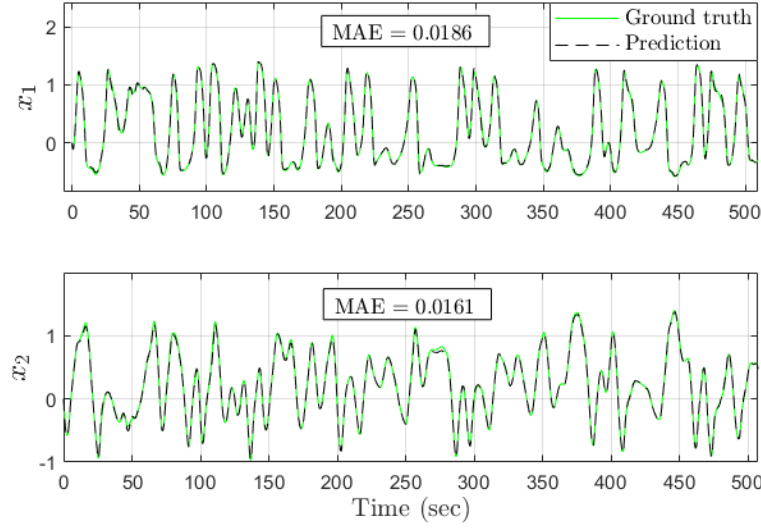


Figure 8. The fitted input-driven dynamics for the first 500 seconds of the validation dataset.

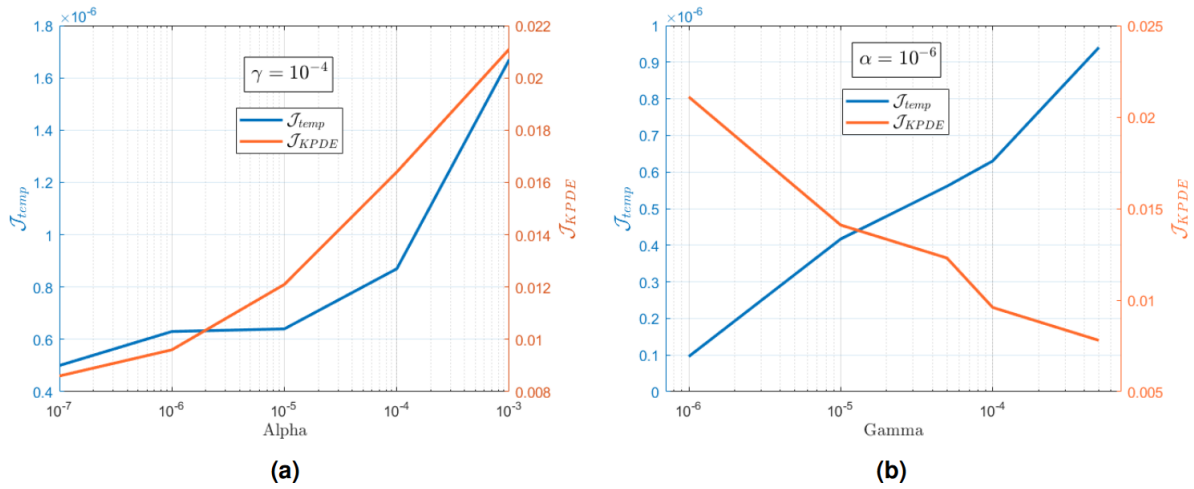


Figure 9. The effect of (a) α and (b) γ on the temporal and KPDE cost terms.

minimization of the temporal cost, whereas the KPDE cost is not significantly affected. The size of the full initial condition grid (evaluated for 11×11 , 21×21 , and 31×31 grids) slightly affects the KPDE cost. Finally, the size of the interpolation grid (evaluated for 50×50 , 75×75 , 100×100 , and 200×200 grids) has the most impact on the computational burden. The KPDE cost grows for the last two cases, as more sample and interpolation points lie in near-edge regions, where the KPDE error is larger.

- (c) **Noise sensitivity.** The effect of noise on the eigenfunction identification phase was analyzed considering additive Gaussian white noise with gradually increasing variance in the range $[10^{-6}, 2.5 \times 10^{-3}]$. The results are shown in Fig. 11. As can be seen, the identification yields good eigenfunctions for noise variance below 6.25×10^{-4} (standard deviation of 0.025). The effect of noise on the shape of eigenfunctions, particularly caused by the drift of initial conditions \mathbf{x}_0 , can be, to some extent, mitigated by decreasing the smoothing parameter of the smoothing spline interpolation. The fitted trajectories are in Supplementary Files.

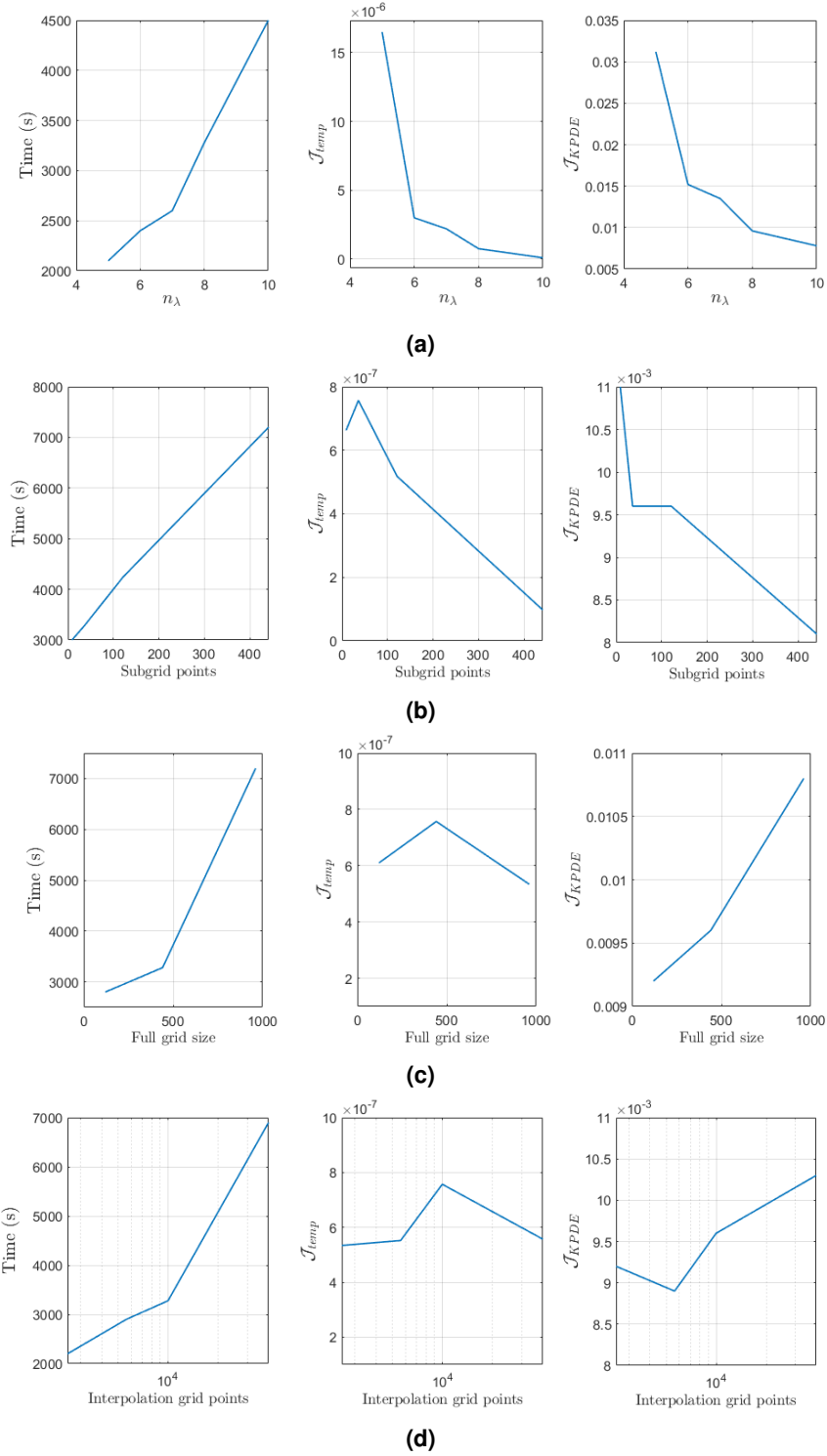


Figure 10. The effect of (a) n_λ , (b) temporal error subgrid size, (c) full grid size, and (d) interpolation grid size on computational time, and temporal and KPDE cost terms.

Limit cycle and isochrons: Van der Pol oscillator

The van der Pol oscillator represents a system characterized by its well-known limit cycle and fast intermittent changes of the state. The system is given as

$$\begin{aligned} \dot{x}_1 &= x_2, \\ \dot{x}_2 &= \mu(1 - x_1^2)x_2 - x_1, \end{aligned} \tag{27}$$

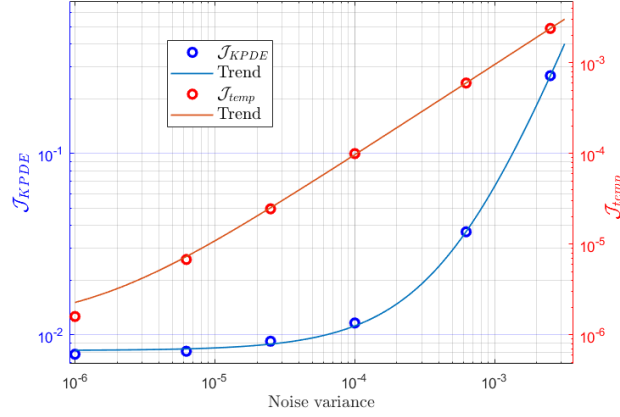


Figure 11. The effect of increasing variance of additive Gaussian white noise on the errors of eigenfunction identification.

where μ is a parameter.

The parameter was set to $\mu = 2$. The system has a characteristic limit cycle in the state space. Despite the simple structure of the system, the discovery of Koopman eigenfunctions poses a challenge. The objective is to find a finite set of complex eigenvalues comprising purely imaginary ones that can accurately represent the limit cycle, and eigenvalues with nonzero real parts explaining the transient phase. The system also exhibits central symmetry, which can be leveraged to speed up the optimization process.

The trajectories were sampled starting from a 21×21 grid in the range of $[-2.5, 2.5] \times [-4, 4]$ to cover the entire limit cycle. The integration time step was $\Delta t = 0.05$ s, and the trajectories were simulated for 10 s (200 samples). The fundamental frequency was estimated from the data as $\omega = 0.824$ rad/s, yielding eigenvalue $\lambda_1 = \pm 0.824i$. The number of additional complex eigenvalues optimized by the algorithm was set to 12. The PSO population size was set to 200, and the number of NM iterations to 1000. Parameters were set as $\alpha = 10^{-6}$ and $\gamma = 10^{-4}$. Interpolation grid size for the identification was 100×100 ($\Delta \mathbf{x} = [0.05, 0.08]$).

The final temporal cost was $J_{temp} = 3.2 \times 10^{-3}$, and the fitted trajectories are plotted in Fig. 12(a). The algorithm placed primary emphasis on the limit cycle, as it is the dominant feature in the training data and therefore has the most significant influence on the temporal cost. At the same time, the reconstruction of the transient phase was less accurate. The level sets of $\angle \phi_1, \lambda_1$, are depicted in Fig. 12(b). As can be seen, the trajectories tend to follow these level sets in the area outside of the limit cycle boundaries. Furthermore, trajectories initialized from the same level set arrive approximately at the same level set after the same time of 1 second (blue solid, blue dashed). This shows simultaneous convergence towards the limit cycle, and thus the level sets represent isochrons, which are equivalent to isostables for limit cycles³⁰. Trajectories starting from the same isochron outside the limit cycle reach the cycle at the same point and remain approximately in phase. These isochrons were computed for a refined grid of 200×200 initial conditions in the range $[-3, 3] \times [-8, 8]$, exceeding the region used for the eigenvalue optimization, which also points at the extrapolation capabilities of the proposed approach.

Ideally, trajectories starting from the same isochron should be in phase on the limit cycle. Since the isochrons are just approximate, the depicted trajectories experienced the following nonzero phase shifts: $\Delta t_{max} = 0.32$ s (black dashed), $\Delta t_{max} = 0.14$ s (red), and $\Delta t_{max} = 0.03$ s (blue). Thus, the phase error grows with the increasing distance the trajectories travel from their corresponding isochrons.

For the other eigenfunctions corresponding to $\lambda_2 = \pm 2.48i$, $\lambda_3 = \pm 4.12i$, $\lambda_4 = \pm 5.78i$, and $\lambda_5 = \pm 7.42i$, the 180-degree phase shift along the limit cycle occurs 3, 5, 7, and 9 times, respectively. Note that the imaginary eigenvalues are approximately given by $\lambda_k = (2k - 1)\lambda_1$, where $\lambda_1 = \pm 0.824i$ corresponds to the fundamental frequency of the limit cycle. This reveals the approximate point spectrum of the limit cycle, which can be further exploited by fixing the set of the most prominent limit-cycle eigenvalues in the population and optimizing additional eigenvalues that should explain the transient convergence phase. An arbitrary number of the limit-cycle eigenvalues can be added using the discovered point spectrum equation.

The initial guess of the first-order fundamental frequency can be approximately observed from the data or made using analytical tools, such as He's frequency formulation or homotopy perturbation methods^{50,51}.

The KPDE comparison for these 4 eigenfunctions is depicted in Fig. 13. Notice the numerical artifacts near the origin, as the unstable fixed point causes singularities in eigenfunctions. The number of spiral branches and valleys increases, corresponding to the integer multiples of the fundamental eigenvalue λ_1 .

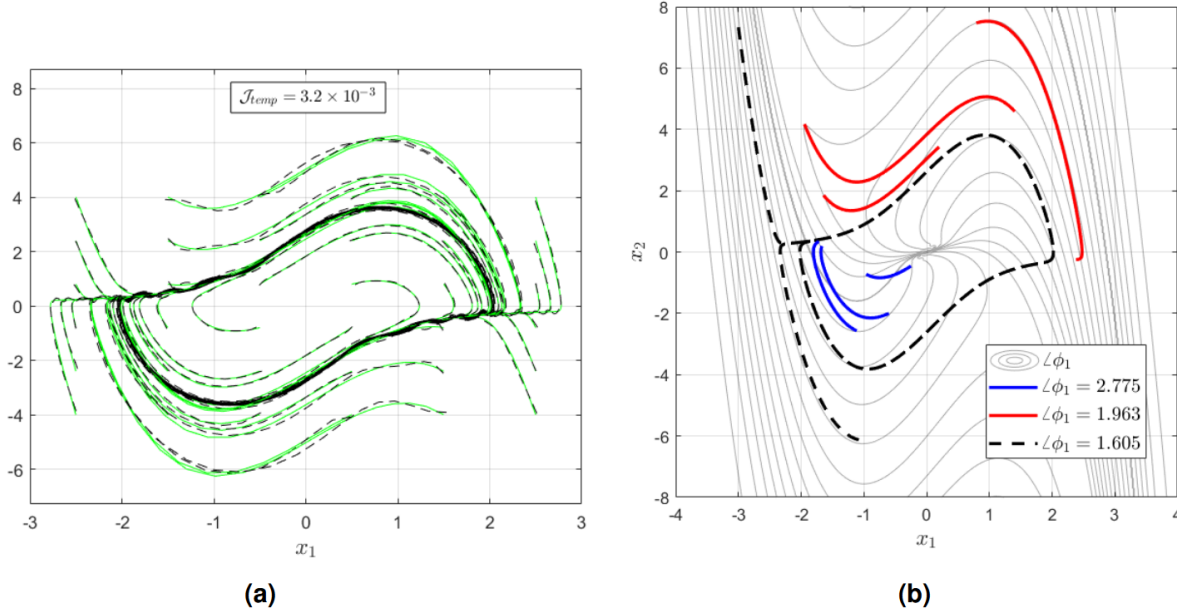


Figure 12. (a) The fitted trajectories in the state space of the van der Pol oscillator - ground truth (green solid) vs. fitted (black dashed). (b) The level sets of $\angle \phi_1 = \arctan(\phi_{1R}/\phi_{1I})$ - trajectories start from the same level set outside (red, black dashed) and inside (blue) the limit cycle, and after the same time, they simultaneously reach another level set.

Invariant subsets: Duffing system

The Duffing oscillator represents a system with multiple fixed points and separable invariant subsets. The system is given as

$$\begin{aligned}\dot{x}_1 &= x_2, \\ \dot{x}_2 &= -\delta x_2 - x_1(b + ax_1^2),\end{aligned}\tag{28}$$

where the parameters were set as $\delta = 0.5$, $a = 1$ and $b = -1$.

With these parameters, the system admits 3 distinct isolated fixed points: two stable at $(-1, 0)$ and $(1, 0)$, and one unstable at $(0, 0)$. The principal eigenvalues of the stable fixed point are $\lambda_{1,2}^s = -0.25 \pm i\sqrt{7.75}/2$, and these of the unstable one are $\lambda_{1,1}^u = 0.781$ and $\lambda_{1,2}^u = -1.281$. The state space is partitioned into two invariant subsets, basins of attraction, corresponding to these points. Once the trajectory starts at one invariant subset, it will stay in it forever. The system also exhibits a global central symmetry, $\mathbf{S}^\tau(\mathbf{x}_0) = -\mathbf{S}^\tau(-\mathbf{x}_0)$, where \mathbf{S}^τ denotes the flow map associated with a trajectory starting from \mathbf{x}_0 after time τ . This symmetry can be exploited for faster learning of the Koopman subspaces¹⁷. Therefore, the identification was performed using only a partial observation of the state space, a grid of 21×21 initial conditions in the right-half plane $[0, 2] \times [-2, 2]$, and the rest of the region of interest was discovered during the fine-tuning step to show the extrapolation capabilities of the framework. Trajectories were simulated for 25 seconds with the integration time step of $\Delta t = 0.05$ s (500 samples).

It is well known that the first eigenfunction acts as an indicator function encoding the information about what invariant subset the points in the state space are located in¹⁷. To promote the presence of this eigenfunction in the set, the $\lambda_0 = 0$ was also included in the population, together with the stable principal eigenvalues, $\lambda_{1,2}^s$ and $\lambda_{1,2}^u$. The total number of eigenvalues was 10, with 7 optimized by the algorithm. The PSO population size was set to 100, and the number of NM iterations was set to 1000. Since the eigenfunctions were expected to contain discontinuous regions near the separatrix, the \mathcal{J}_{KPDE} term was tuned down, and only the temporal part of the optimization was utilized. The upper bound for real parts was set to -0.3 . The resulting temporal cost was $\mathcal{J}_{temp} = 6.2 \times 10^{-6}$ and the fitted trajectories are depicted in Fig. 14.

The indicator function nature of the conservative eigenfunction ϕ_0 is evident from Fig. 15 (matching the results in references^{9,17}). The S-shaped boundary between the invariant sets is called a separatrix.

For illustration, another identification was performed keeping the same settings but with $\gamma = 10^{-6}$. The resulting errors were $\mathcal{J}_{KPDE} = 1.53$ and $\mathcal{J}_{KPDE} = 0.508$ for training and refinement, respectively. The absolute value of the KPDE residual is plotted in Fig. 16 for the training (a) and the refined solution (b). During the training, the peaks were located near the separatrix. Refinement moved the peaks to the edges as the accuracy of gradient computation and separatrix location improved.

Fig. 17 shows the isostables that match the EDMD results reported in Williams et al.⁹ and denoted by the red squares (only shapes for reference, the contour levels are not aligned). Two trajectories starting from the same level set $|\phi_1| = 0.717$

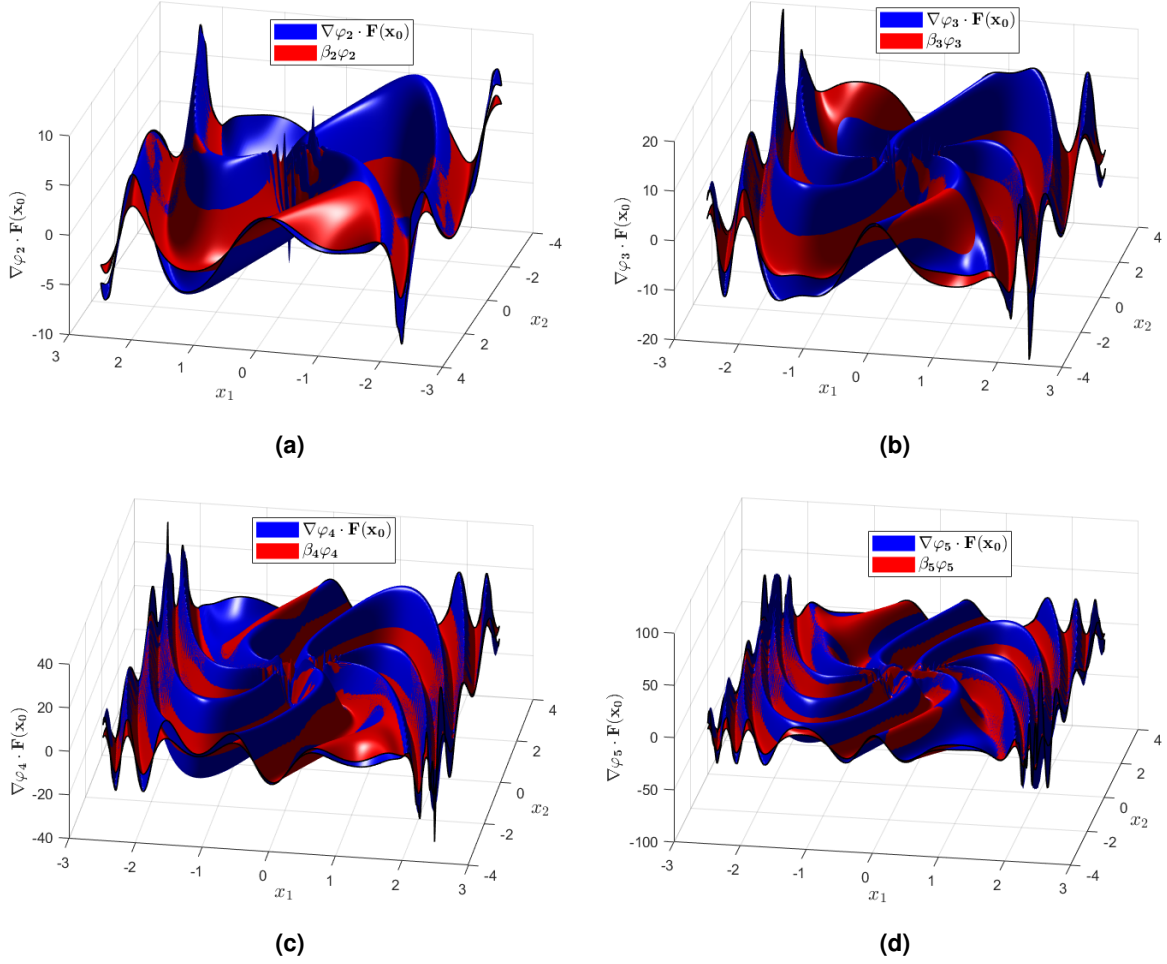


Figure 13. Comparison of LHS (blue) and RHS (red) of the KPDE for eigenfunctions $\varphi_{2,\dots,5}$ of the van der Pol oscillator. The corresponding imaginary part are (a) $\pm 2.48i$, (b) $\pm 4.12i$, (c) $\pm 5.78i$, and (d) $\pm 7.42i$.

simultaneously arrive at level sets $|\varphi_1| = 0.4$ and $|\varphi_1| = 0.21$ after 2.5 and 5 seconds, respectively, pointing at the level sets approximating the isostables accurately. Isostables and isochrons of φ_1 can be used for parameterization of the basins of attraction⁹ and conversion to action-angle coordinates for control³⁰. Note that the separatrix is also apparent for nonzero eigenvalues, but it is slightly blurred.

Unknown dynamics and control: 2-spool turbojet(fan) engine

The two-spool turbojet engine represents a complex nonlinear dissipative system. It is a control nonaffine system, and thus the effects of control cannot be easily decoupled and must be included in the learning process. Also, it is an example of a system with unknown dynamics, where it is even challenging to measure the autonomous trajectories due to practical reasons. Here, the engine serves as an example system with practical implications. It operates in a subspace of the state space bounded by safety limits corresponding primarily to surge, over-pressure in the combustion chamber, combustor blowout, and over-temperature in the high-pressure turbine^{52,53}.

An input-driven trajectory was simulated using a reference nonlinear physics-based component-level model based on the GasTurb simulation software⁵⁴. This trajectory observed the majority of the operating region of the engine, meeting the upper and lower limits of its operation. A Gaussian white noise was added to the signals, and normalization to the $[0, 1]$ range was performed. The underlying governing equations for spool speeds N_1 and N_2 were discovered using the SINDy approach with linear and logistic functions as a basis, and nonlinear parameter learning. Additionally, the solution was penalized for nonzero values in the origin since it is favorable to avoid shifting of the fixed point. The mentioned models and procedures are explained

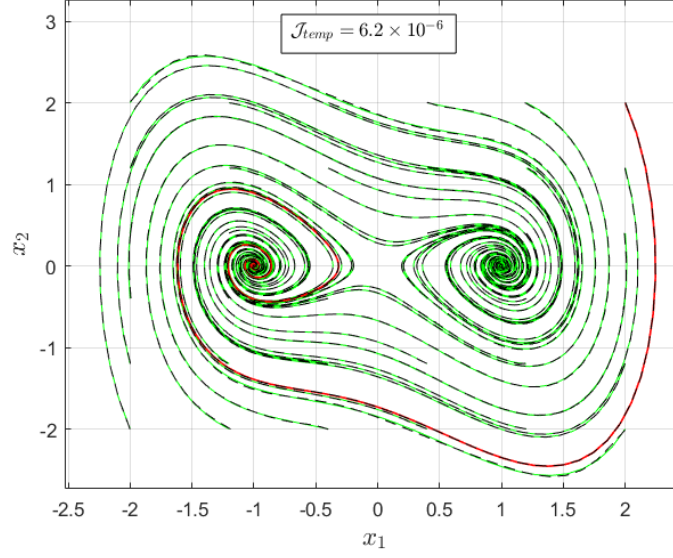


Figure 14. Fitted trajectories in the state space of the dissipative Duffing system - ground truth (green solid) vs. fitted (black dashed), and the reference trajectory (red).

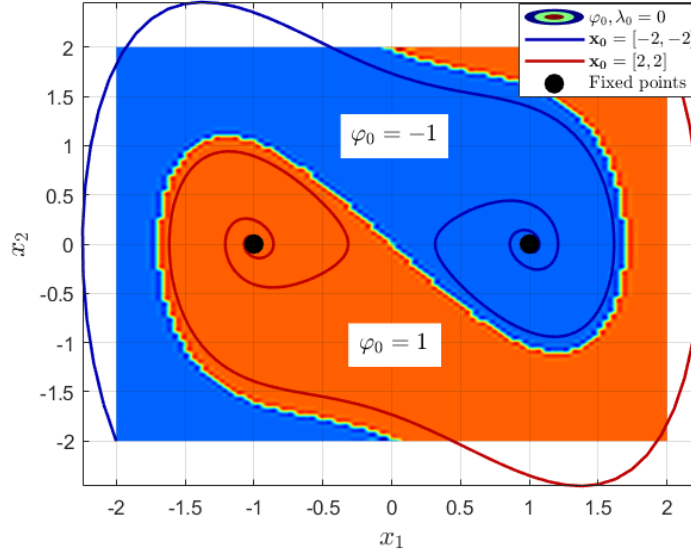


Figure 15. The first conservative eigenfunction, φ_0 , uncovering the 2 invariant subsets corresponding to the two stable fixed points with a characteristic S-shaped separatrix.

in the reference⁸. The model was simplified to a control-affine structure given as

$$\begin{bmatrix} \dot{N}_1 \\ \dot{N}_2 \end{bmatrix} = \begin{bmatrix} f_1 \\ f_2 \end{bmatrix} + \begin{bmatrix} g_{11} & g_{12} \\ g_{21} & g_{22} \end{bmatrix} \begin{bmatrix} W_f \\ A_n \end{bmatrix}, \quad (29)$$

where N_1 and N_2 are the normalized low-pressure and high-pressure rotor speeds, respectively, W_f and A_n are the fuel flow and nozzle area, f_1 and f_2 are the autonomous dynamics functions, and g_{11} , g_{12} , g_{21} and g_{22} are the input dynamics functions respectively, all functions of N_1 and N_2 .

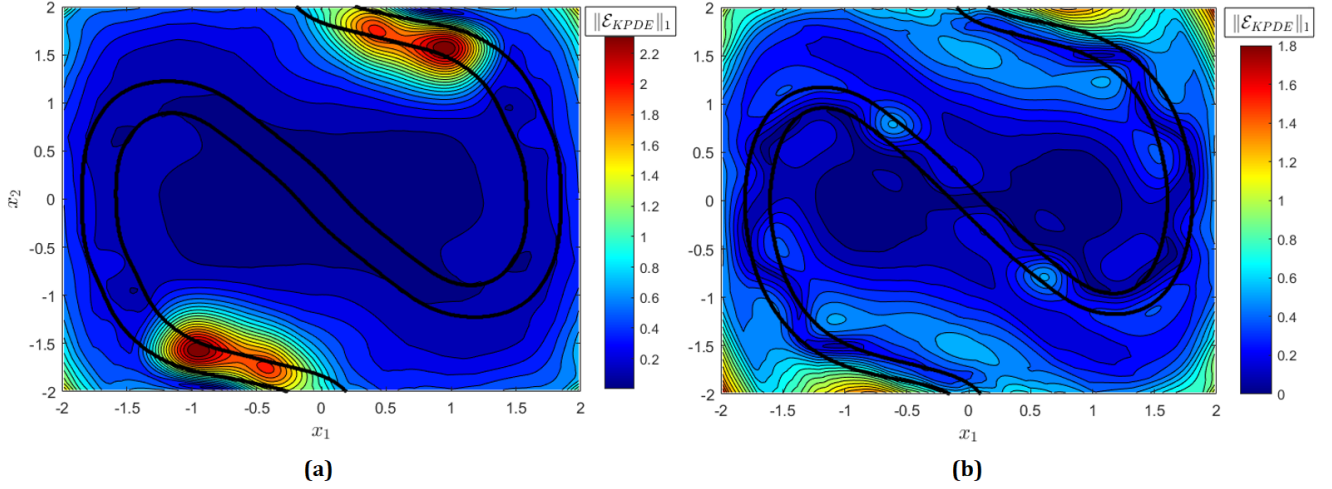


Figure 16. Absolute values of KPDE residuals w.r.t. the separatrix for (a) the training and (b) the refined solution. Black solid lines indicate the vicinity of the separatrix.

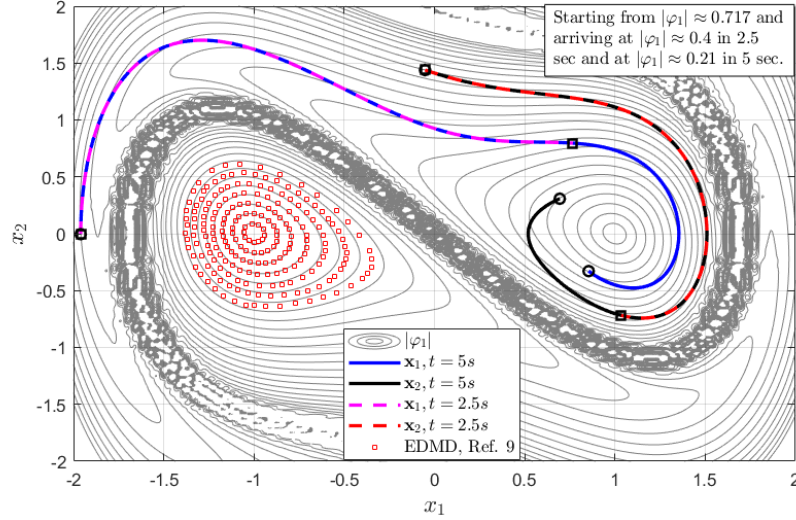


Figure 17. Level sets of $|\varphi_1|$ giving the isostables of both stable fixed points of the Duffing system. Two trajectories starting from the same level set approached another level set after the same time. The times were 2.5 sec (blue and black dashed lines) and 5 sec (cyan and violet solid lines). Red squares denote the isostables obtained by EDMD⁹.

Eigenfunction identification

Only the autonomous dynamics, obtained by $u = 0$, were further considered for the generation of the trajectories for the eigenfunction identification. The trajectories were simulated from a grid of 21×21 initial conditions in the range $[-0.1, 1.1] \times [-0.1, 1.1]$ to cover possible overshoots causing the controlled trajectory to leave the normalization region. The trajectories were 3 seconds long, and the integration time step was $\Delta t = 0.01$ s (300 samples). Since the distance of the fixed point, corresponding to the idle regime of engine operation, to the origin was negligible, no shift was needed. The principal eigenvalues obtained from the linearization at the origin were $\lambda_{1,2} = -2.835 \pm 1.19i$. Four additional complex eigenvalues were considered for the identification. The PSO population size was set to 50, and the number of NM iterations was set to 1000. The regularization and KPDE weights were $\alpha = 10^{-6}$ and $\gamma = 10^{-4}$, respectively. Interpolation grid size for the identification was 100×100 ($\Delta \mathbf{x} = [0.012, 0.012]$).

The algorithm discovered 4 complex eigenvalues with the final temporal cost of $\mathcal{J}_{temp} = 1.67 \times 10^{-7}$. The total number of eigenfunctions was thus 10. The results for the autonomous trajectory reconstruction are depicted in Fig. 18.

Fig. 19 shows the comparison of the first 4 KPDE terms, exhibiting satisfying agreement.

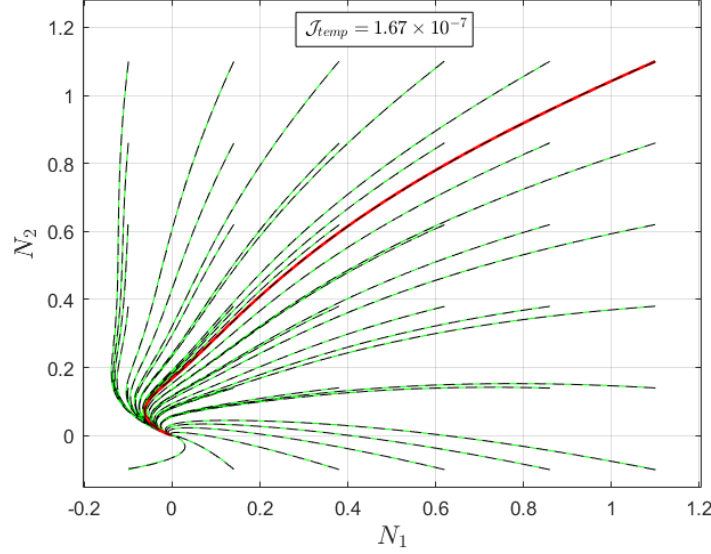


Figure 18. Fitted autonomous trajectories and the temporal cost of the 2-spool GTE. Ground truth (green solid) vs. fit (black dashed), and the reference trajectory (red).

After the refinement step, using a grid of 100×100 initial conditions and 500×500 interpolation grid ($\Delta \mathbf{x} = [0.0024, 0.0024]$), the numerically estimated gradient was utilized to compute the input dynamics, $\nabla \Phi \cdot \mathbf{G}$, which were subsequently approximated by a linear combination of 15 sigmoid basis functions as

$$\nabla \Phi \cdot \mathbf{G} \approx \Gamma(\mathbf{x}) = \mathbf{W}_2 \sigma(\mathbf{w}_1^T \mathbf{x} + \mathbf{b}_1) + \mathbf{B}_2, \quad (30)$$

where \mathbf{w}_1 , \mathbf{b}_1 , \mathbf{W}_2 and \mathbf{B}_2 are the input weights, input biases, output weights and output biases, respectively, and $\sigma = f(\hat{N}_1, \hat{N}_2)$ is the sigmoid function given by (26), where $\hat{(\cdot)}$ denotes the estimate.

This approximation covered the interaction with both inputs using the same basis for all 20 entries. Similar to the FitzHugh-Nagumo system, the optimization of sigmoid parameters and output weights was carried out using the MATLAB Deep Learning Toolbox, where the model was represented by a single-hidden-layer network with a linear output layer. The validation results are plotted in Fig. 20. As can be seen, the input-driven trajectory was predicted with good accuracy ($\sum \text{MAE} = 40.07$ RPM).

For jet engines in particular, the reconstruction of other quantities, e.g., thrust, turbine inlet temperature, surge margin, etc., is of interest. For demonstration purposes, the results of a projection of these quantities onto the augmented space of eigenfunctions and inputs are presented in Fig. 21.

Kalman filter design

Subsequently, the Kalman filter was designed to estimate the eigenfunction state vector, avoiding the expensive computation of the eigenfunction interpolants. Details about the design are in Supplementary Methods. The predicted spool speeds were treated as a mean observation, $\mu(\mathbf{x}) \approx \mathbf{C}\Phi(t)$, for estimation of the measurement noise covariance matrix as $\mathbf{w}_n \sim \mathcal{N}(0, \Sigma_{\mathbf{x}}^2)$: $\Sigma_{\mathbf{x}}^2 = \text{Cov}(\mathbf{x} - \mu(\mathbf{x}))$. Alternatively, the measurement noise can be directly estimated from a real steady-state measurement.

Furthermore, to deal with the process noise, $\mathbf{w}_p \sim \mathcal{N}(0, \Sigma_{\mathbf{p}}^2)$, the eigenfunctions were evaluated using the filtered ground-truth states, \mathbf{x}_{filt} , and compared to the mean eigenfunction dynamics prediction, $\mu(\dot{\Phi}) \approx \dot{\Phi}(t)$, to estimate the process noise covariance as

$$\Sigma_{\mathbf{p}}^2 \approx \text{Cov} \left(\frac{\Phi(\mathbf{x}_{\text{filt}})^+ - \Phi(\mathbf{x}_{\text{filt}})^-}{\Delta t} - \mu(\dot{\Phi}) \right), \quad (31)$$

where $\Phi(\mathbf{x}_{\text{filt}})^+$ and $\Phi(\mathbf{x}_{\text{filt}})^-$ are the forward and backward values used for the central difference approximation of ground-truth time derivatives, respectively.

Based on these estimates, the \mathbf{Q}_0 and \mathbf{R}_0 observer weighting matrices were tuned, and the optimal Kalman gain matrix was obtained by solving the observer algebraic Riccati equation. More details about observer design can be found, e.g., in⁴².

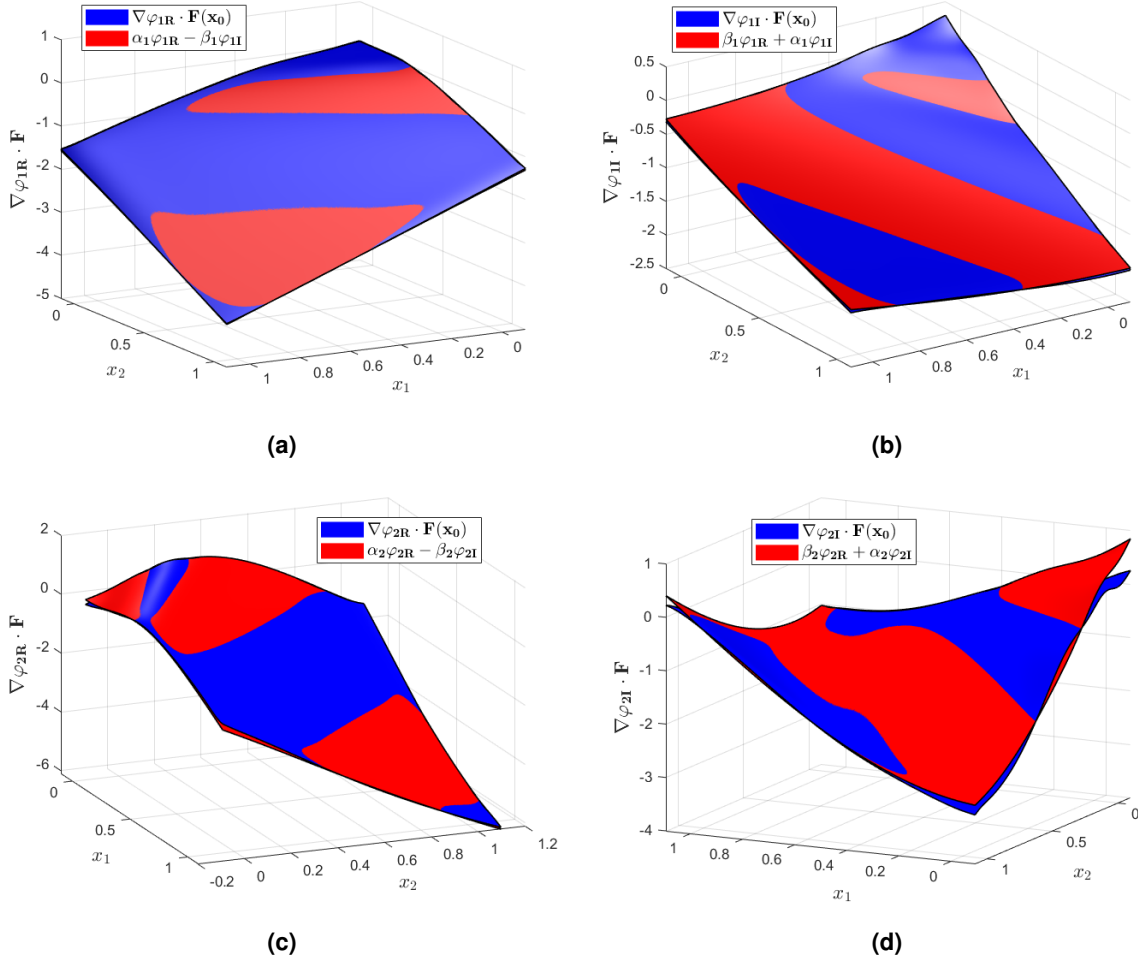


Figure 19. Comparison of LHS (blue) and RHS (red) of the KPDE terms for the first 4 eigenfunctions of the 2-spool GTE. The corresponding eigenvalues are (a,b) $\lambda_{1,2} = -2.835 \pm 1.19i$ and (c,d) $\lambda_{3,4} = -2.85 \pm 3.29i$.

Gain-scheduled optimal spool-speed controller design

Using the data assimilation with the KF, the prediction accuracy was increased, and the spool speed measurement noise was attenuated. Finally, a state-dependent gain-scheduled tracking linear quadratic regulator (LQR) was designed. It should be noted that this article is not primarily focused on jet engine control. Thus, this serves solely as an example of the utilization of the Koopman framework for the design of optimal tracking controllers in the eigenfunction space, leveraging the linear output relations. However, the control framework with Koopman observer and LQG control with integral action for a GTE was discussed in detail in our previous work⁸, and the currently implemented design is described in Supplementary Methods. The control of N_1 and N_2 using both control inputs was assumed. The controller also accounted for the actuator dynamics modeled as first-order lags⁵³:

$$\begin{bmatrix} \dot{W}_f \\ \dot{A}_n \end{bmatrix} = \begin{bmatrix} -\frac{1}{T_f} & 0 \\ 0 & -\frac{1}{T_a} \end{bmatrix} \begin{bmatrix} W_f \\ A_n \end{bmatrix} + \begin{bmatrix} \frac{1}{T_f} & 0 \\ 0 & \frac{1}{T_a} \end{bmatrix} \begin{bmatrix} W_f^{comm} \\ A_n^{comm} \end{bmatrix}, \quad (32)$$

where $T_f = 0.06$ s and $T_a = 0.1$ s are the fuel system and nozzle time constants, respectively, and superscript $(\cdot)^{comm}$ denotes the controller commands.

These two linear state equations were augmented with the eigenfunction model, yielding a 12th-order system. The scheduling parameters were the spool speeds. The operating region was sampled at a discrete set of points, and the input dynamics were evaluated at each point, yielding a locally LTI system coherent with the underlying dynamics. The locally optimal LQR gain matrix was subsequently obtained at each point by solving the LQR Riccati equation⁴². The eigenfunction weight matrix was set as $\mathbf{Q}_\Phi = \mathbf{C}^T \mathbf{Q}_x \mathbf{C}$, where $\mathbf{Q}_x = \text{diag} [5 \ 5]$, yielding a distribution of spool speed error penalization

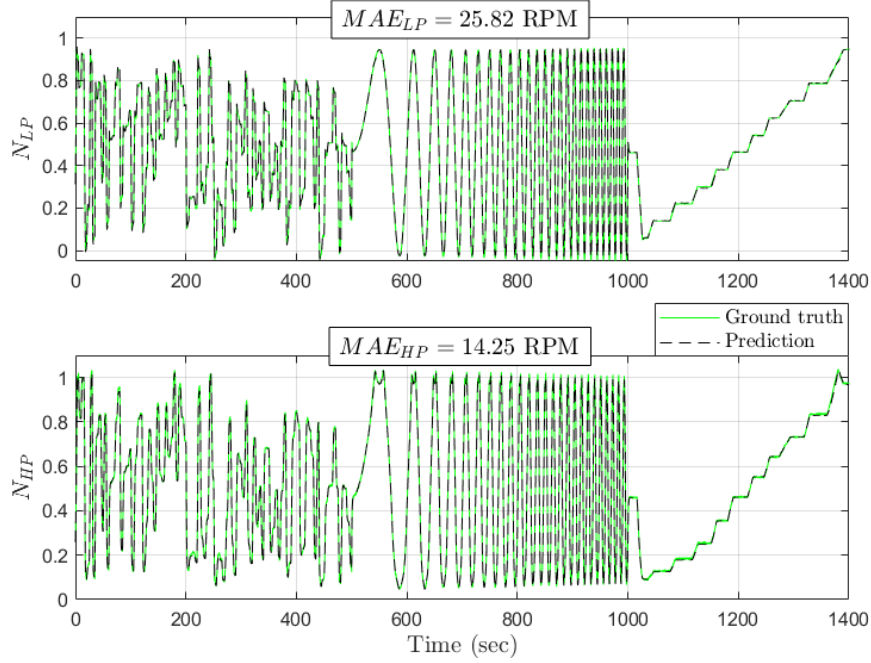


Figure 20. Fitted input-driven dynamics of the 2-spool GTE with the corresponding mean absolute errors.

among eigenfunctions, and the input weight matrix was set as $\mathbf{R} = \text{diag}[0.5 \ 0.1]$, penalizing mainly the fuel consumption.

Subsequently, the gains were projected onto the input dynamics basis. Since it is already computed for the Koopman KF prediction update, and the landscapes of the input dynamics directly affect the gain landscapes, the gain matrix can be regressed using the same basis. This way, the computational cost is decreased as it is not needed to compute two individual sets of basis functions. The resulting control law for the commanded inputs, \mathbf{u}_{comm} , was given as follows:

$$\mathbf{u}_{\text{comm}} = \mathbf{u}_{\text{ss}} - \mathbf{K}_{\Phi}(\hat{\Phi} - \Phi_{\text{ss}}) - \mathbf{K}_{\mathbf{W}\mathbf{A}}(\mathbf{u} - \mathbf{u}_{\text{ss}}) - \mathbf{K}_{\mathbf{i}}\boldsymbol{\eta}, \quad (33)$$

where $(\cdot)_{\text{ss}}$ denotes the desired steady-state values, $\hat{\Phi}$ are the eigenfunction estimates given by the KF, $\mathbf{u} = [W_f \ A_n]^T$ now denotes the actual measured fuel flow and nozzle area (i.e., the actuator states) as given by (32), $\boldsymbol{\eta} = [\int_0^t (N_1^{\text{set}} - N_1) d\tau \ \int_0^t (N_2^{\text{set}} - N_2) d\tau]^T$ is a vector of the tracking error integrals, and $[\mathbf{K}_{\Phi} \ \mathbf{K}_{\mathbf{W}\mathbf{A}}] = \mathbf{K}_{\text{LQR}}$ and $\mathbf{K}_{\mathbf{i}}$ are the LQR gain matrix and diagonal integral-state gain matrix, respectively.

The LQR gain matrix can be written as

$$\mathbf{K}_{\text{LQR}} = \mathbf{W}_{\mathbf{K}}\boldsymbol{\sigma}(\hat{N}_1, \hat{N}_2) + \mathbf{B}_{\mathbf{K}}, \quad (34)$$

where $\mathbf{W}_{\mathbf{K}}$ and $\mathbf{B}_{\mathbf{K}}$ are the weights and biases of the control law, respectively, and $\boldsymbol{\sigma}$ is the same as in (30).

The steady-state terms are obtained as

$$\begin{bmatrix} \Phi_{\text{ss}} \\ \mathbf{u}_{\text{ss}} \end{bmatrix} = \begin{bmatrix} \Lambda & \Gamma(\hat{N}_1, \hat{N}_2) \\ \mathbf{C}_{\text{ref}} & \mathbf{0} \end{bmatrix}^{-1} \begin{bmatrix} \mathbf{0} \\ \mathbf{x}_{\text{r}} \end{bmatrix}, \quad (35)$$

where $\mathbf{x}_{\text{r}} = [N_1^{\text{set}} \ N_2^{\text{set}}]^T$ is the setpoint vector.

It should be noted that the tracking LQR is very sensitive to model uncertainties, as the allocation of the steady-state values is completely dependent on the model matrices. Therefore, an integral action was introduced to the control law, rendering it more robust. A similar approach, based on solving the Riccati equation for the eigenfunctions augmented with an integral of the tracking error, can be utilized to form a linear quadratic integrator^{8,55,56}. In this example, the integral gain matrix, $\mathbf{K}_{\mathbf{i}}$, was tuned manually and kept diagonal for a decoupled control, so that W_f depends primarily on the N_2 tracking error, and A_n depends primarily on the N_1 tracking error. This reflects the thermodynamic effects in the engine⁵². The gains were optimized as $\mathbf{K}_{\mathbf{i}} = \text{diag}[0.5 \ 0.5]$. The LQR weight matrices and the integral gains can be optimized for a specified setpoint profile using, e.g., a metaheuristic optimization.

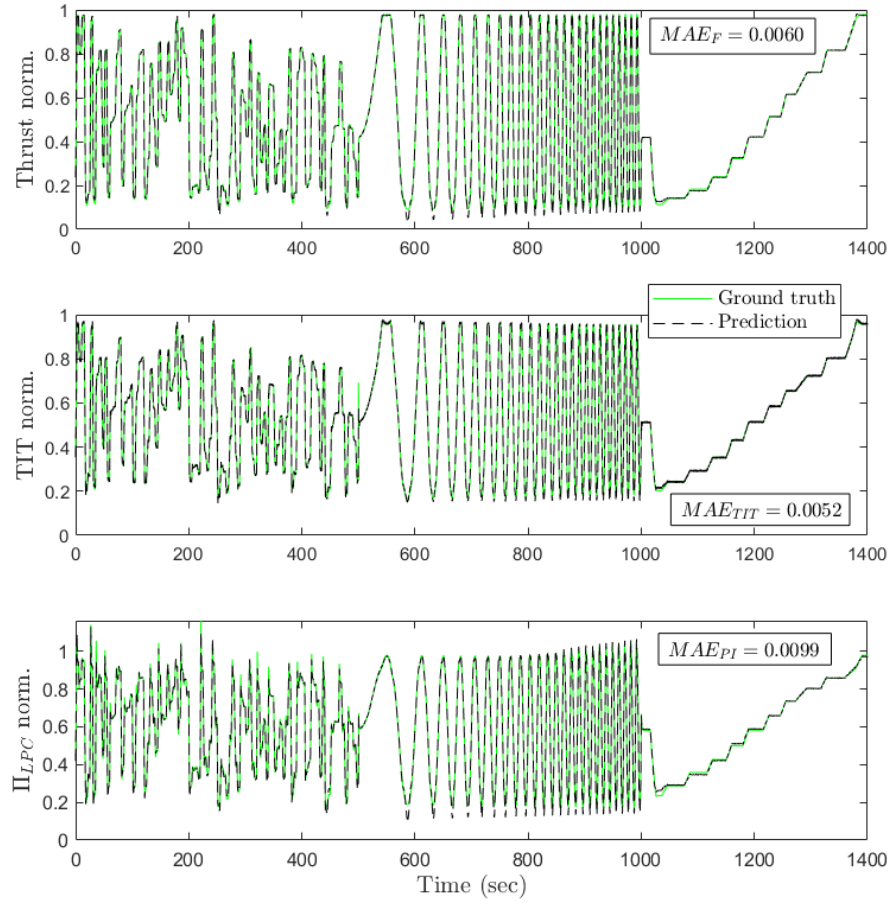


Figure 21. Fitted example output variables of the 2-spool GTE: a) thrust, b) turbine inlet temperature, and c) low-pressure compressor pressure ratio.

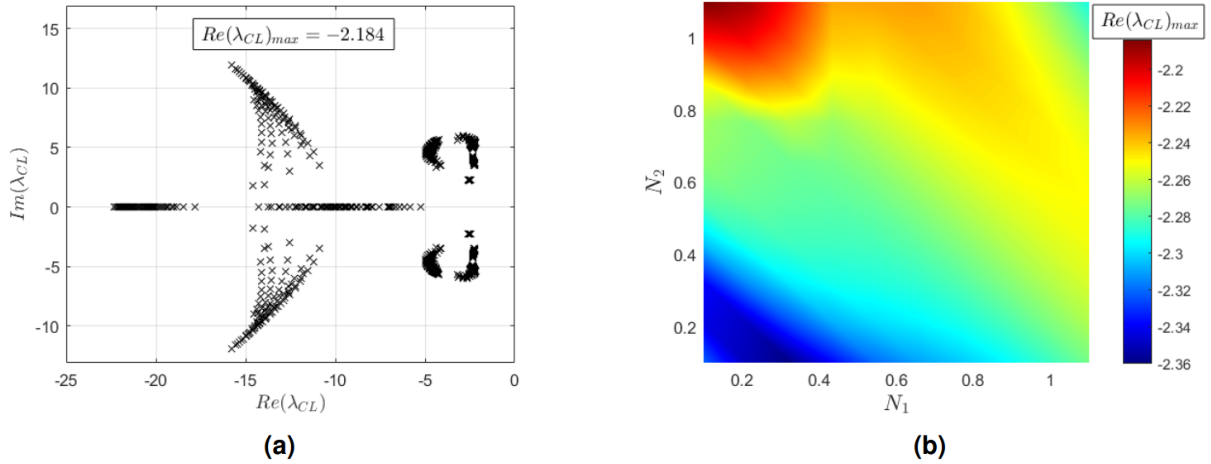


Figure 22. The closed-loop eigenvalues, Λ_{CL} : (a) distribution in the complex plane, and (b) maximum real parts vs. N_1 and N_2 .

The eigenvalues of the closed-loop system matrix were checked at all grid points. The maximum real value was $\Re(\lambda_{CL})_{max} = -2.184$, yielding a safe stability margin. The eigenvalues are shown in Fig. 22.

The controller was connected to a limiter with a min-max selector that ensures input saturation, preventing exceeding the operational limits corresponding, e.g., to surge, over-temperature, etc. The clamping anti-windup technique was employed to

interrupt the integration of control errors during saturation. For more details on jet engine control systems and this configuration, the reader can be directed to references^{8,53}.

Results for the spool-speed gain-scheduled tracking LQG

The example results for comparison to a classical proportional-integral (PI) controller are depicted in Fig. 23. The quantitative comparison of thrust settling times and overshoots, and spool speed overshoots is in Table 1. The PI controller gains for relative physical spool speeds (no normalization, only division by design values) were $K_{p,1} = 0.5$ and $K_{i,1} = 1$ for N_1 , and $K_{p,2} = 20$, $K_{i,2} = 30$ for N_2 . The Koopman tracking LQG controller outperforms the PID, especially in the N_2 control, ultimately leading to an overall better thrust response with acceptable overshoots (below 5 %). The PID control is additionally burdened by a coupling between the individual loops, giving rise to a need for a sufficient decoupling strategy, increasing the complexity of the control design. The figure also shows the prediction of the Koopman Kalman estimator. The prediction accuracy of both spool speeds is satisfactory. The thrust prediction is acceptable for the acceleration, whereas during deceleration, it significantly diverges near the minimum value.

It should be noted that to obtain better performance using the PI controller, one would have to implement gain scheduling and design the controller around multiple operating points that are restricted to the steady-state operating line⁵³. In the Koopman framework, the optimal control design was significantly simplified to a single selection of weight matrices, and the controller is optimal in the entire operating region.

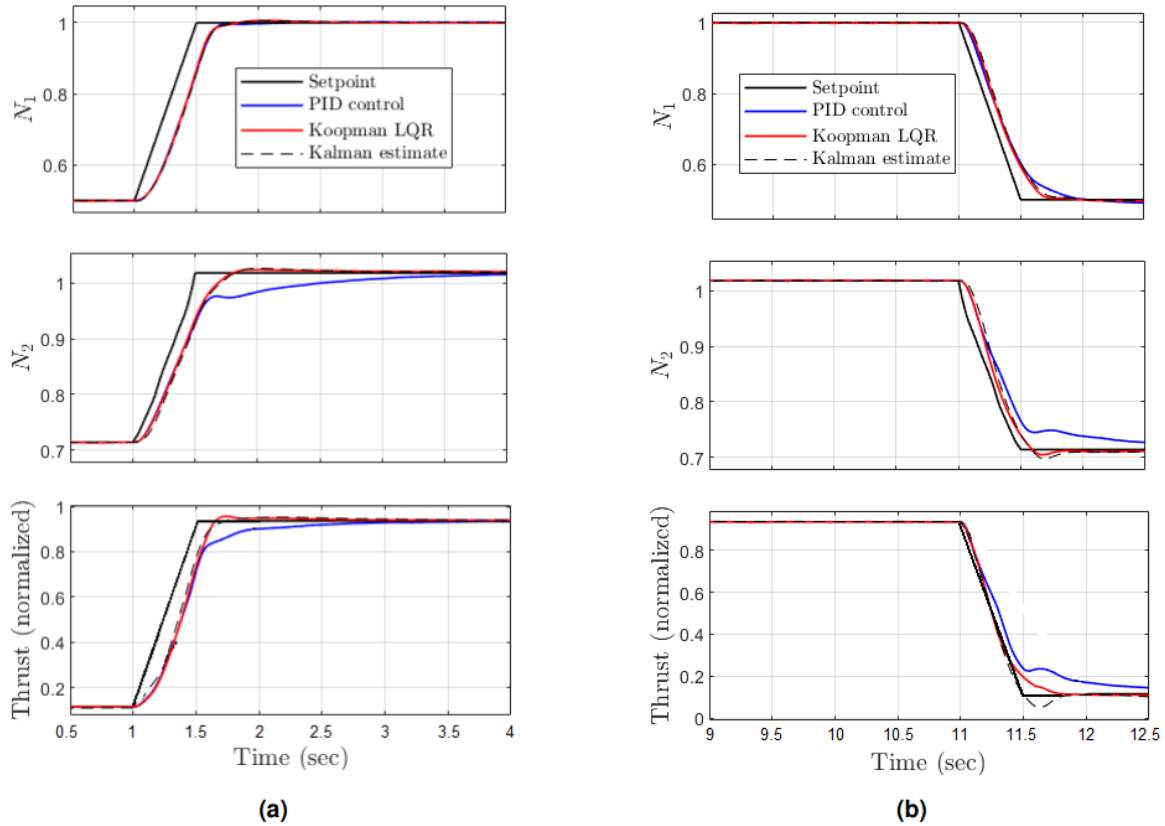


Figure 23. Example of tracking LQG (red) performance compared to a PID controller (blue) for (a) acceleration and (b) deceleration of the 2-spool GTE. The black dashed lines correspond to the KF estimates for N_1 and N_2 , and to the Koopman prediction of thrust.

Fig. 24 shows the comparison of control inputs. As can be seen, the LQR controller utilized both fuel flow and nozzle area efficiently to achieve good thrust response, especially regarding the swift nozzle area changes as the spool speeds reached the setpoint.

Since the parameter-varying input dynamics are in an affine form, they can be easily converted to a polytopic form, and the analysis and control synthesis can be performed in the vertices. Thanks to the properties of convex sets, ensuring a stable and optimal behavior at vertices renders the system optimal everywhere in the bounded parameter space⁵⁷. The robust nonlinear approaches, e.g., discussed in reference³⁷, can also be applied to the Koopman LPV.

Table 1. Comparison of PID and Koopman gain-scheduled tracking LQG controllers. The thrust settling times were assessed for $\pm 2\%$ of the step size (0.821).

Controller	$t_{\pm 2\% \Delta F}^{acc}$	$t_{\pm 2\% \Delta F}^{dec}$	F acc. OS	F acc. OS	N_1 acc. OS	N_1 dec. OS	N_2 acc. OS	N_2 dec. OS
PID	1.55 s	2.02 s	0.00 %	-0.00 %	0.48 %	-2.30 %	0.00 %	-0.00 %
LQG	0.79 s	0.70 s	2.46 %	-0.77 %	1.23 %	-0.81 %	1.97 %	-3.00 %

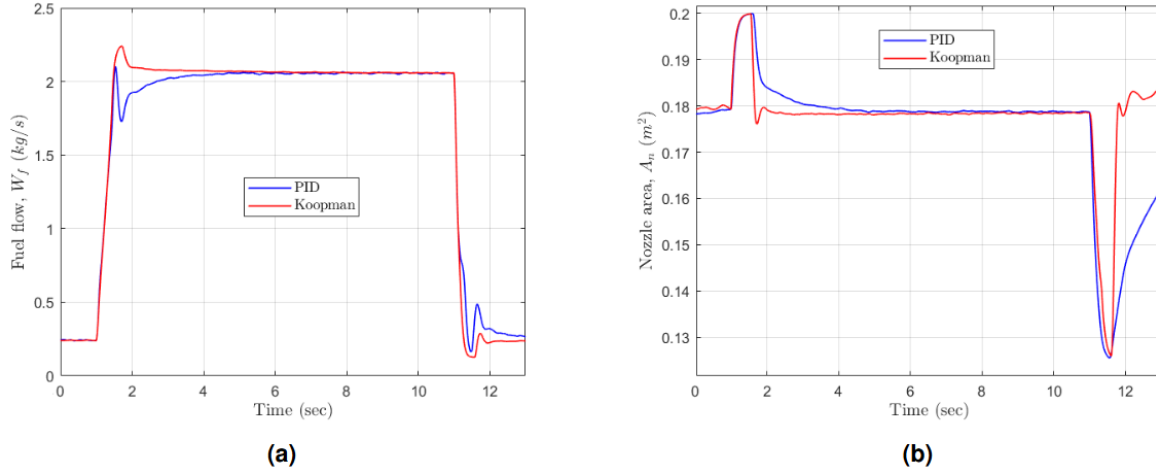


Figure 24. Comparison of (a) the fuel flow and (b) the nozzle area commanded by both controllers.

Conclusion

This paper proposed a new approach to dictionary-free discovery of Koopman eigenfunctions from data using optimal mapping from the space of initial conditions of a set of autonomous trajectories of the nonlinear system to the space of initial conditions of eigenfunctions, Φ , such that all the nonlinear trajectories can be projected onto the linear evolution of Φ . The method utilizes a notion of a reference trajectory and fixed reference Koopman modes with a subsequent transformation of the temporal basis, projection onto which represents the optimal initial conditions Φ_0 . Since the eigenfunctions are rendered based on the given eigenvalues, both are optimized simultaneously using the PSO. Additionally, the interpolation and numerical differentiation of Φ_0 can be used for the computation of the KPDE cost function, further forcing the optimized eigenvalues to render functions with reasonable spatial structure.

The dictionary-free approach offers more freedom in the identification compared, e.g., to EDMD methods, where the structure of eigenfunctions is restricted to the span of observables chosen for the lifting, and spurious eigenpairs are often present in the set. The eigenfunction formulation further allows for designing eigenvalues to target specific features of the system, such as limit cycles, which means there will be at least one purely imaginary eigenvalue associated with the cycle's fundamental frequency, or fixed points outside the origin, indicating a conservative mode with a zero eigenvalue.

The approach was tested on several benchmark nonlinear models. The results point to the ability of the approach to represent both dissipative and conservative systems with multiple fixed points and limit cycles. Particularly interesting are features of the systems' state-space geometry, like isostables and isochrons. For the van der Pol oscillator, the isochrons and the relation between the approximate limit cycle point spectrum and the spatial structure of eigenfunctions (branches) were discussed. The method can also discover invariant subsets in the state space associated with multiple fixed points and a zero eigenvalue. For systems without discontinuous regions in eigenfunctions, the KPDE integrity promotion proved to help generate good eigenfunctions. The addition of the principal eigenvalues significantly improves the solution. Furthermore, the symmetry can be exploited to construct eigenfunctions using only partial observations of the state space, which was shown for the Duffing system.

The approach also provides a tool for estimation of the input dynamics, utilizing the numerical gradient and subsequent regression. The input dynamics fitting and optimal control design were showcased for the example of a 2-spool turbojet GTE, where both spool speeds were effectively controlled using both inputs - fuel flow and nozzle area. The gain-scheduled Koopman LQG controller outperformed the classical PID controller while being relatively easy to design. Other observable quantities, namely thrust, LPC pressure ratio, and HPT inlet total temperature, were also successfully projected onto the span of

eigenfunctions and inputs.

Among the disadvantages of the approach is the requirement for relatively dense sampling of the state space to supply enough trajectories for an efficient eigenfunction discovery. However, the number of trajectories is on par with other approaches from the literature (100s of trajectories). Associated with this is also a longer computational time of the closed-loop optimization, especially using population-based algorithms like PSO. However, this is primarily a hardware-dependent problem that can be partially resolved by further optimizing the code. For a given set of eigenvalues, the eigenfunction discovery is performed in a matter of seconds. For 4- and higher-dimensional systems, setting up the KPDE computation might be laborious. Furthermore, the KPDE cost function is sensitive to the quality of the interpolation process, and the approach is sensitive to the choice of the reference trajectory, especially when the trajectory does not capture the main dynamical characteristics of the system.

In future research, applications to higher-dimensional systems, like dissipative Lorenz systems, flow around a cylinder²², chaotic systems⁵⁸, or a 3-spool turbofan engine, will also be investigated, as well as extensions to multi-agent or distributed systems. The current version utilizes smoothing-spline interpolation and 3rd-order accuracy central differences to compute the gradient. Also, the analytical differentiation of the spline interpolant might be tested, as well as automatic reference trajectory selection based on relevant coverage metrics.

Furthermore, the potential direct thrust control for GTEs might be investigated, using the linear thrust reconstruction and the corresponding Koopman modes for a simple optimal/adaptive LQG design. The thrust could be estimated using some other, more accurate method providing in-flight thrust feedback. This estimator should be trained on flight data to capture the effect of the flight Mach number. The algorithm should also be tested in varying flight conditions. This approach paves the way for a simpler data-driven discovery of eigenfunctions.

Data availability

Codes and datasets supporting the results can be found in the supplementary materials. Additional materials will be made available upon reasonable request.

References

1. Koopman, B. O. Hamiltonian systems and transformations in hilbert space. *Proc. Natl. Acad. Sci. United States Am.* **17**, 315–318 (1931).
2. Koopman, B. O. & Neumann, J. V. Dynamical systems of continuous spectra. *Proc. Natl. Acad. Sci. United States Am.* **18**, 255–263 (1932).
3. Brunton, S. L. & Kutz, J. N. *Data-Driven Science and Engineering: Machine Learning, Dynamical Systems, and Control* (Cambridge University Press, Cambridge, 2019).
4. Mauroy, A., Mezić, I. & Susuki, Y. (eds.) *The Koopman Operator in Systems and Control* (Springer Nature, Cham, Switzerland, 2020).
5. Surana, A. Koopman Operator Framework for Time Series Modeling and Analysis. *J. Nonlinear Sci.* **30**, 1973–2006, DOI: [10.1007/s00332-017-9441-y](https://doi.org/10.1007/s00332-017-9441-y) (2020).
6. Brunton, S. L., Budišić, M., Kaiser, E. & Kutz, J. N. Modern koopman theory for dynamical systems. *SIAM Rev.* **64**, 229–340, DOI: [10.1137/21M1401243](https://doi.org/10.1137/21M1401243) (2022).
7. Kaiser, E., Kutz, J. N. & Brunton, S. L. Data-driven discovery of koopman eigenfunctions for control. *Mach. Learn. Sci. Technol.* **2**, 035023, DOI: [10.1088/2632-2153/abf0f5](https://doi.org/10.1088/2632-2153/abf0f5) (2021).
8. Grasev, D. Identification and optimal nonlinear control of turbojet engine using koopman eigenfunction model, DOI: <https://doi.org/10.48550/arXiv.2505.10438> (2025).
9. Williams, M., Kevrekidis, I. & Rowley, C. A data-driven approximation of the koopman operator: Extending dynamic mode decomposition. *J Nonlinear Sci* **25**, 1307–1346, DOI: <https://doi.org/10.1007/s00332-015-9258-5> (2015).
10. Williams, M. O., Rowley, C. W. & Kevrekidis, I. G. A kernel-based method for data-driven koopman spectral analysis. *J. Comput. Dyn.* **2**, 247–265, DOI: <https://doi.org/10.3934/jcd.2015005> (2015).
11. Jiang, W., Zhang, X. I., Zuo, Z., Shi, M. & Su, S. Data-driven kalman filter with kernel-based koopman operators for nonlinear robot systems. In *2022 IEEE/RSJ International Conference on Intelligent Robots and Systems (IROS)*, 12872–12878, DOI: [10.1109/IROS47612.2022.9981408](https://doi.org/10.1109/IROS47612.2022.9981408) (2022).
12. Ishikawa, I., Hashimoto, Y., Ikeda, M. & Kawahara, Y. Koopman operators with intrinsic observables in rigged reproducing kernel hilbert spaces, DOI: <https://doi.org/10.48550/arXiv.2403.02524> (2024).

13. Jovanović, M. R., Schmid, P. J. & Nichols, J. W. Sparsity-promoting dynamic mode decomposition. *Phys. Fluids* **26**, 024103, DOI: [10.1063/1.4863670](https://doi.org/10.1063/1.4863670) (2014).
14. Schlosser, C. & Korda, M. Sparsity structures for koopman and perron–frobenius operators. *SIAM J. on Appl. Dyn. Syst.* **21**, 2187–2214, DOI: [10.1137/21M1466608](https://doi.org/10.1137/21M1466608) (2022).
15. Klus, S. *et al.* Data-driven approximation of the koopman generator: Model reduction, system identification, and control. *Phys. D: Nonlinear Phenom.* **406**, 132416, DOI: <https://doi.org/10.1016/j.physd.2020.132416> (2020).
16. Colbrook, M. J., Ayton, L. J. & Szöke, M. Residual dynamic mode decomposition: robust and verified koopmanism. *J. Fluid Mech.* **955**, A21, DOI: [10.1017/jfm.2022.1052](https://doi.org/10.1017/jfm.2022.1052) (2023).
17. Pan, S. & Duraisamy, K. On the lifting and reconstruction of nonlinear systems with multiple invariant sets. *Nonlinear Dyn.* **112**, 10157–10165, DOI: [10.1007/s11071-024-09581-0](https://doi.org/10.1007/s11071-024-09581-0) (2024).
18. Proctor, J. L., Brunton, S. L. & Kutz, J. N. Generalizing koopman theory to allow for inputs and control. *SIAM J. on Appl. Dyn. Syst.* **17**, 909–930, DOI: [10.1137/16M1062296](https://doi.org/10.1137/16M1062296) (2018).
19. Brunton, S. L., Brunton, B. W., Proctor, J. L., Kaiser, E. & Kutz, J. N. Chaos as an intermittently forced linear system. *Nat. Commun.* **8**, 19, DOI: [10.1038/s41467-017-00030-8](https://doi.org/10.1038/s41467-017-00030-8) (2017).
20. Li, X. *et al.* Data-driven koopman learning and prediction of piezoelectric tube scanner hysteresis. *IEEE Transactions on Syst. Man, Cybern. Syst.* **54**, 3631–3641, DOI: [10.1109/TSMC.2024.3368570](https://doi.org/10.1109/TSMC.2024.3368570) (2024).
21. Takeishi, N., Kawahara, Y. & Yairi, T. Learning koopman invariant subspaces for dynamic mode decomposition. *CoRR abs/1710.04340*, DOI: <https://doi.org/10.48550/arXiv.1710.04340> (2017).
22. Lusch, B., Kutz, J. & Brunton, S. L. Deep learning for universal linear embeddings of nonlinear dynamics. *Nat Commun* **9**, 4950, DOI: <https://doi.org/10.1038/s41467-018-07210-0> (2018).
23. Li, Y., He, H., Wu, J., Katabi, D. & Torralba, A. Learning compositional koopman operators for model-based control. In *International Conference on Learning Representations* (2020).
24. Jin, Y., Hou, L. & Zhong, S. Extended dynamic mode decomposition with invertible dictionary learning. *Neural Networks* **173**, 106177, DOI: <https://doi.org/10.1016/j.neunet.2024.106177> (2024).
25. Grasev, D. Data-driven identification of gas turbine engine dynamics via koopman operator genetic algorithm. *IEEE Access* **13**, 91972–91988, DOI: [10.1109/ACCESS.2025.3573472](https://doi.org/10.1109/ACCESS.2025.3573472) (2025).
26. Johnson, C. A. & Yeung, E. A class of logistic functions for approximating state-inclusive koopman operators. In *2018 Annual American Control Conference (ACC)*, 4803–4810, DOI: [10.23919/ACC.2018.8431525](https://doi.org/10.23919/ACC.2018.8431525) (2018).
27. Mezić, I. Spectrum of the koopman operator, spectral expansions in functional spaces, and state-space geometry. *J Nonlinear Sci* **30**, 2091–2145, DOI: <https://doi.org/10.1007/s00332-019-09598-5> (2020).
28. Mezić, I. Analysis of fluid flows via spectral properties of the koopman operator. *Annu. Rev. Fluid Mech.* **45**, 357–378, DOI: <https://doi.org/10.1146/annurev-fluid-011212-140652> (2013).
29. Brunton, S. L., Brunton, B. W., Proctor, J. L. & Kutz, J. N. Koopman invariant subspaces and finite linear representations of nonlinear dynamical systems for control. *PLOS ONE* **11**, 1–19, DOI: [10.1371/journal.pone.0150171](https://doi.org/10.1371/journal.pone.0150171) (2016).
30. Mauroy, A., Mezić, I. & Moehlis, J. Isostables, isochrons, and koopman spectrum for the action–angle representation of stable fixed point dynamics. *Phys. D: Nonlinear Phenom.* **261**, 19–30, DOI: <https://doi.org/10.1016/j.physd.2013.06.004> (2013).
31. Liu, Y., Sholokhov, A., Mansour, H. & Nabi, S. Physics-informed koopman network, DOI: <https://doi.org/10.48550/arXiv.2211.09419> (2022).
32. Kingma, D. P. & Ba, J. Adam: A method for stochastic optimization, DOI: <https://doi.org/10.48550/arXiv.1412.6980> (2015).
33. Korda, M. & Mezić, I. Optimal construction of koopman eigenfunctions for prediction and control. *IEEE Transactions on Autom. Control.* **65**, 5114–5129, DOI: [10.1109/TAC.2020.2978039](https://doi.org/10.1109/TAC.2020.2978039) (2020).
34. Cibulka, V., Korda, M. & Haniš, T. Dictionary-free koopman model predictive control with nonlinear input transformation. *SIAM J. on Appl. Dyn. Syst.* **24**, 94–130, DOI: [10.1137/23M1597174](https://doi.org/10.1137/23M1597174) (2025).
35. Hoerl, A. E. & Kennard, R. W. Ridge regression: Biased estimation for nonorthogonal problems. *Technometrics* **12**, 55–67, DOI: <https://doi.org/10.2307/1267352> (1970).

36. Bagheri, S. *Analysis and control of transitional shear flows using global modes*. Ph.D. thesis, Department of Mechanics, Royal Institute of Technology, Stockholm, Sweden (2010).
37. Rigatos, G. *et al.* Nonlinear optimal control for a gas compressor driven by an induction motor. *Results Control. Optim.* **11**, 100226, DOI: <https://doi.org/10.1016/j.rico.2023.100226> (2023).
38. Zhang, X., Pan, W., Scattolini, R., Yu, S. & Xu, X. Robust tube-based model predictive control with koopman operators. *Automatica* **137**, 110114, DOI: <https://doi.org/10.1016/j.automatica.2021.110114> (2022).
39. Zhou, J., Jia, Y. & Sun, C. Flywheel energy storage system controlled using tube-based deep koopman model predictive control for wind power smoothing. *Appl. Energy* **381**, 125117, DOI: <https://doi.org/10.1016/j.apenergy.2024.125117> (2025).
40. Campi, M. & Kumar, P. Optimal adaptive control of an lqg system. In *Proceedings of 35th IEEE Conference on Decision and Control*, vol. 1, 349–353 vol.1, DOI: [10.1109/CDC.1996.574332](https://doi.org/10.1109/CDC.1996.574332) (1996).
41. Annaswamy, A. M. & Fradkov, A. L. A historical perspective of adaptive control and learning. *Annu. Rev. Control.* **52**, 18–41, DOI: <https://doi.org/10.1016/j.arcontrol.2021.10.014> (2021).
42. Friedland, B. *Control System Design* (Dover Publications, Mineola, NY, 1987).
43. Brunton, S. L., Proctor, J. L. & Kutz, J. N. Discovering governing equations from data by sparse identification of nonlinear dynamical systems. *Proc. Natl. Acad. Sci.* **113**, 3932–3937, DOI: [10.1073/pnas.1517384113](https://doi.org/10.1073/pnas.1517384113) (2016).
44. Sengupta, B., Friston, K. & Penny, W. Efficient gradient computation for dynamical models. *NeuroImage* **98**, 521–527, DOI: <https://doi.org/10.1016/j.neuroimage.2014.04.040> (2014).
45. Kennedy, J. & Eberhart, R. Particle swarm optimization. In *Proceedings of ICNN'95 - International Conference on Neural Networks*, vol. 4, 1942–1948, DOI: [10.1109/ICNN.1995.488968](https://doi.org/10.1109/ICNN.1995.488968) (1995).
46. Nelder, J. A. & Mead, R. A simplex method for function minimization. *Comput. J.* **7**, 308–313, DOI: [10.1093/COMJNL/7.4.308](https://doi.org/10.1093/COMJNL/7.4.308) (1965).
47. White, A. P., Zhu, G. & Choi, J. *Linear Parameter-Varying Control for Engineering Applications* (Springer London, 2013).
48. Vafamand, N., Asemani, M. H., Mobayen, S. & Pujol-Vázquez, G. Robust polytopic-lpv body-weight-dependent control of blood glucose in type-1 diabetes. *IEEE Access* **9**, 96367–96379, DOI: [10.1109/ACCESS.2021.3095216](https://doi.org/10.1109/ACCESS.2021.3095216) (2021).
49. Huang, T. *et al.* Polytopic lpv modeling and gain scheduling hinf control of ball screw with position- and load-dependent variable dynamics. *Precis. Eng.* **87**, 1–10, DOI: <https://doi.org/10.1016/j.precisioneng.2024.01.004> (2024).
50. He, J.-H. Some asymptotic methods for strongly nonlinear equations. *Int. J. Mod. Phys. B* **20**, 1141–1199, DOI: <https://doi.org/10.1142/S0217979206033796> (2006).
51. He, J.-H., Jiao, M.-L., Gepreel, K. A. & Khan, Y. Homotopy perturbation method for strongly nonlinear oscillators. *Math. Comput. Simul.* **204**, 243–258, DOI: <https://doi.org/10.1016/j.matcom.2022.08.005> (2023).
52. Mattingly, J. D. & Boyer, K. M. *Elements of Propulsion: Gas Turbines and Rockets, Second Edition* (American Institute for Aeronautics and Astronautics, Reston, Virginia, 2016).
53. Jaw, L. C. & Mattingly, J. D. *Aircraft Engine Controls: Design, System Analysis, And Health Monitoring* (Amer Inst Aero & Astro, Reston, Virginia, 2009).
54. Kurzke, J. *GasTurb 13: Design and Off-Design Performance of Gas Turbines*. GasTurb GmbH, Aachen, Germany (2018). Available at <https://www.gasturb.com/Downloads/Manuals/GasTurb12.pdf>.
55. Pand, S., Jafari, S., Nikolaidis, T. & Li, Q. A novel model-based multivariable framework for aircraft gas turbine engine limit protection control. *Chin. J. Aeronaut.* **34**, 57–72, DOI: <https://doi.org/10.1016/j.cja.2021.04.002> (2021).
56. Zhu, Y., Huang, J., Pan, M. & Zhou, W. Direct thrust control for multivariable turbofan engine based on affine linear parameter-varying approach. *Chin. J. Aeronaut.* **35**, 125–136, DOI: <https://doi.org/10.1016/j.cja.2021.09.018> (2022).
57. Liu, Z., Huang, Y., Gou, L. & Fan, D. A robust adaptive linear parameter-varying gain-scheduling controller for aeroengines. *Aerosp. Sci. Technol.* **138**, 108319, DOI: <https://doi.org/10.1016/j.ast.2023.108319> (2023).
58. Gao, S. *et al.* A three-dimensional memristor-based hyperchaotic map for pseudorandom number generation and multi-image encryption. *Chaos* **35**, 073105, DOI: [10.1063/5.0270220](https://doi.org/10.1063/5.0270220) (2025).

Funding

The author declares that this research was supported by funding provided by the Ministry of Defence and the Ministry of Education, Youth and Sports of the Czech Republic.

Author contributions statement

The author confirms sole responsibility for the following: study conception and design, simulation and data collection, analysis and interpretation of results, and manuscript preparation.

Additional information

Conflict of interest

The author has no conflicts of interest and no relevant financial or non-financial interests to disclose.